

1 Time varying changes and uncertainties in the CMIP6 ocean carbon sink from global ~~to regional~~ 2 to local scale

3 Parsa Gooya¹, Neil C. Swart^{2,1}, Roberta C. Hamme¹

4 ¹School of Earth and Ocean Sciences, University of Victoria, Victoria, BC, V8P 5C2, Canada

5 ²Canadian Centre for Climate Modelling and Analysis, Environment and Climate Change Canada, Victoria, BC,
6 V8W 2P2, Canada

7 *Correspondence to:* Parsa Gooya (parsa.g76@gmail.com)

8 **Abstract.** As a major sink for anthropogenic carbon, the oceans slow the increase of carbon dioxide in the
9 atmosphere and regulate climate change. Future changes in the ocean carbon sink, and its uncertainty at a global
10 and regional scale, are key to understanding the future evolution of the climate. Here, we ~~conduct a multimodel~~
11 ~~analysis of report on~~ the changes and uncertainties in the historical and future ocean carbon sink using output ~~data~~
12 from the ~~latest phase of the~~ Coupled Model Intercomparison Project- Phase 6 (CMIP6), multimodel ensemble and
13 ~~observations compare to one observation based product~~. We show that the ocean carbon sink is concentrated in
14 highly active regions - 70 percent of the total sink occurs in less than 40 percent of the global ocean. High pattern
15 correlations between the historical and projected future carbon sink indicate that future uptake will largely continue
16 to occur in historically important regions. We conduct a detailed breakdown of the sources of uncertainty in the
17 future carbon sink by region. Scenario Consistent with CMIP5 models, scenario uncertainty dominates at the global
18 scale, followed by model uncertainty, and then internal variability. We demonstrate how the importance of internal
19 variability increases moving to smaller spatial scales and go on to show how the breakdown between scenario,
20 model, and internal variability changes between different ocean basins regions, governed by different processes.
21 Moreover, Using the CanESM5 large ensemble we show that internal variability changes with time based on the
22 scenario, breaking the widely employed assumption of stationarity. As with the mean sink, we show that uncertainty
23 in the future ocean carbon sink is also concentrated in the known regions of historical uptake. ~~The resulting~~
24 ~~patterns~~ Patterns in the signal-to-noise ratio have ~~strong~~ implications for observational detectability and time of
25 emergence, which ~~varies~~ we show to vary both in space and with scenario. ~~Our~~ We show that the largest variations
26 in emergence time across scenarios occurs in regions where ocean sink is less sensitive to forcing - outside of the
27 highly active regions. In agreement with CMIP5 studies, our results suggest that to detect ~~human influence~~
28 ~~on changes in~~ the ocean carbon sink as early as possible, and to efficiently reduce uncertainty in future carbon

29 uptake, modelling and observational efforts should be focused in the known regions of high historical uptake,
30 including the Northwest Atlantic and the Southern Ocean.

31 1. Introduction

32 Recent increases in greenhouse gases have trapped additional heat relative to the pre-industrial era and raised
33 Earth's average temperature. Carbon dioxide (CO₂) is the primary driver of ~~the~~ global warming in the industrial
34 period (Masson-Delmotte et al., 2021). The concentration of atmospheric CO₂ has increased from approximately
35 277 parts per million (ppm) in 1750 (Joos et al., 2008), the beginning of the Industrial Era, to 409 ppm in 2019.
36 However, less than half of the CO₂ emitted by anthropogenic ~~CO₂-activity~~ has remained in the atmosphere; ~~the~~.
37 The remaining CO₂ ~~has been~~ was taken up by the natural carbon sinks of the ocean and the terrestrial biosphere.
38 Specifically, the global ocean absorbed ~26% of the total CO₂ emissions during 2011-2020 (Friedlingstein et al.,
39 2021).

40
41 The ocean's capacity to absorb ~~increasing amounts of~~ anthropogenic CO₂ is not uniformly distributed (McKinley
42 et al., 2016, Sarmiento et al., 1998). Despite increasing atmospheric CO₂ concentrations, the air-sea CO₂ flux does
43 not change much in the subtropical gyres. The regions where ocean carbon uptake notably increases are those with
44 strong exchange between the surface and the deep ocean (Ridge and McKinley, 2021; Frölicher et al., 2015;
45 McKinley et al., 2016). This response of the ocean carbon sink to increasing atmospheric CO₂ levels consists
46 of changes in both the anthropogenic and the natural carbon sink (Crisp et al. 2022, McKinley et al. 2020,
47 Hauk et al., 2020, Gruber et al. 2019, Frolicher at al, 2015). Even within regions there are large variations in the
48 ~~sink. The Northeast Pacific, for instance, is a net sink for atmospheric CO₂. However, the region includes diverse~~
49 ~~oceanographic areas such as open ocean, continental margins, and fjords, leading to large spatial variability~~
50 ~~in dominant mechanisms and~~ the direction of the ~~CO₂ sea-air flux (Sutton et al., 2017; Takahashi et al., 2006)-carbon~~
51 ~~sink~~. In the Southern Ocean, for instance, the spatial superposition of natural and anthropogenic CO₂ fluxes leads
52 to a relatively strong uptake band between approximately 55°S and 35°S (Gruber et al., 2019). However, south of
53 the Polar Front (55°S), the different estimates agree less well (Gruber et al., 2019). Supported by measurements
54 based on biogeochemical floats (Bushinsky et al., 2019; Gray et al., 2018; Williams et al., 2018), Gruber et al.
55 (2019) ~~argues~~ argue that the region was most likely a small source in 2019.

56

57 Earth System Models (ESMs) are the primary tool for projecting the future evolution of ~~ocean carbon uptake on~~
58 ~~subannual to centennial timescales in the climate system~~. However, quantitative projections from ESMs ~~across these~~
59 ~~timescales~~ are subject to considerable uncertainty, particularly at regional and local scales (Friedrich et
60 al., 2012; Frölicher et al., 2014; Hauck et al., 2015; Laufkötter et al., 2015; Roy et al., 2011; Tjiputra et al., 2014;
61 Terhaar et al., 2021) where less averaging is done and ~~more diverse~~ different individual mechanisms dominate
62 different regions. Projection uncertainty varies with lead time, spatial averaging scale, and from region to region:
63 (Lovenduski et al., 2016; Schlunegger et al., 2020). For example, Lovenduski et al. (2016) showed a spatially
64 heterogeneous pattern of projection uncertainty in CO₂ flux projections over 17 ocean regions; for CMIP5 models.
65 Furthermore, by comparing uncertainty at the global scale to the scale of the California Current System, they show
66 that uncertainty was relatively is higher compared to the global scale. If at smaller scales. Schlunegger et al. (2020)
67 further shows different partitioning of uncertainty for 10 ocean basins at the year 2050. All said, if ESMs are
68 to be used to quantify future changes in ocean carbon uptake, especially across shorter timescales and at regional
69 spatial scales, and to inform observational campaign planning, their uncertainties must be well known and well
70 understood (Lovenduski et al., 2016).

71
72 A systematic characterization of projection uncertainty has become possible with the advent of the Coupled Model
73 Intercomparison Project (CMIP), as a number of climate models of similar complexity provided simulations over
74 a consistent time period and with the same set of emissions scenarios (Lehner et al., 2020). ~~We consider~~ There are
75 three main types of ~~projection~~ uncertainty in climate model projections, as described by Hawkins and Sutton (2009)
76 (hereafter HS09):

77
78 **Uncertainty due to internal variability:** Internal variability is the unforced natural climate variability resulting
79 from the internal processes in the climate system. Modes such as the El Niño–Southern Oscillation, North Atlantic
80 Oscillation, Atlantic Multidecadal Oscillation, Pacific Decadal Oscillation, and Southern Annular Mode (SAM)
81 contribute, ~~along with others~~, to this internal variability. Internal variability also includes variability that acts on
82 shorter time and spatial scales, such as submesoscale and mesoscale ocean features (Frolicher et al., 2016). The
83 real world follows only one of an infinite possible number of *realizations* of internal variability, and due to its
84 chaotic nature, the future evolution of internal variability is not predictable beyond short timescales. (Somerville,
85 1987; Lorenz, 1969). Climate model simulations do not attempt to reproduce the exact observed evolution of
86 internal variability, but produce their own, unique realizations that aim to capture the correct statistics of this
87 variability. Hence, our analysis must account for internal variability, both when comparing historical model

88 simulations to observations, and when considering uncertainties in the future ocean carbon sink. In HS09, a fourth-
89 order polynomial fit to simulated global and regional temperature timeseries represented the forced response, while
90 the residual from this fit represented the internal variability. ~~However~~ There is thus, an assumption of stationarity
91 (constant in time) in their method. ~~Moreover~~, this approach could possibly conflate internal variability with the
92 forced response in cases where low-frequency (decadal-to-multidecadal) internal variability exists, or when the
93 forced signal is weak, which makes the statistical fit a poor estimate of the forced response (Kumar and Ganguly,
94 2018). In this study, we instead use a Single-Model Initial-condition Large Ensemble (SMILE) to robustly quantify
95 the ~~simulated forced response and~~ internal variability across time and scenarios using ensemble statistics (Lehner
96 et al., 2020). A SMILE is an ensemble of model realizations that each starts from different initial conditions but
97 uses the same model and forcing, and provides representations of the climate system that are equivalent except for
98 internal variability.

99 **Uncertainty due to model structure:** ~~Each model has a specific way of representing the physical world.~~ Models
100 differ in their resolution, structure, numerics, and parameterization of processes. These differences cause models
101 to respond differently to the same forcing. For example, the CMIP5 model simulations run under Representative
102 Concentration Pathway 8.5 (RCP8.5) project a wide range of cumulative anthropogenic carbon storage by 2100
103 (320–635 Pg-C) (Ciais and Sabine, 2013) due to both internal variability and model uncertainty (Lovenduski et al.,
104 2016).

105 **Uncertainty due to emission scenario:** The future of the climate system depends on human activity and our
106 emission of climate active gases that change radiative forcing. Future emissions are highly uncertain, given our
107 inability to project the complex changes in society and technology upon which they depend. As a result, future
108 simulations are run with a range of possible “scenarios” for how future emissions (or atmospheric concentrations)
109 will evolve under different socioeconomic storylines. These scenarios are prescribed via the internationally
110 coordinated experiments organized by the Coupled Model Intercomparison Project. Since the future emission
111 trajectory is unknown, these future simulations are referred to as projections, rather than predictions. Projections
112 of future ocean carbon uptake from ESMs are greatly influenced by the choice of emission scenario (Lovenduski
113 et al., 2016). For example, cumulative ocean carbon uptake from 1850 is projected to saturate at approximately 290
114 ± 30 GtC under ssp126, and to reach 520 ± 40 GtC by 2100 under ssp585 for CMIP6 models (Canadell et al.,
115 2021). ~~the cumulative oceanic storage of anthropogenic carbon in CMIP5 models by 2100 ranges from 110–220 Pg-~~
116 ~~C under RCP2.6 to 320–635 Pg C under RCP8.5 (Ciais and Sabine, 2013).~~

117 ~~In this paper we~~ Together with the patterns of changes in the sink, the patterns of internal variability allow for an
118 assessment of the required timescales for detection of changes in the ocean carbon sink. Detection means that we
119 can robustly separate the forced signal from internal variability (McKinley et al., 2016). Detectability can be
120 assessed using Time of Emergence (TOE; Hawkins and Sutton, 2012; Lovenduski et al., 2016; McKinley et al.,
121 2016; Rodgers et al., 2015; Schlunegger et al., 2020 & 2019). For example, McKinley et al. (2016) and Schlunegger
122 et al. (2019) showed that the forced signal of increasing ocean carbon uptake is not detectable in the Ekman
123 convergence regions of the subtropical gyres. Schlunegger et al. (2020) builds on that using four large ensembles
124 of CMIP5 ESM simulations with two forcing scenarios to show that air-sea CO₂ flux TOEs show strong agreement
125 between the large-ensembles not just for global and regional scales but also locally and spatially. Their use of only
126 four models and two scenarios however, potentially underestimates the contribution of model and scenario
127 uncertainty.

128
129 Here, we build on previous work using CMIP6 models. We make use of an ensemble of 13 models to better capture
130 model uncertainty in the response to different forcing (scenarios) and three scenarios to represent a wider range of
131 future possibilities including a strong mitigation scenario. We start by analysing the regional patterns of historical
132 ocean carbon uptake and how they are projected to change in the future (Sect. 3.1). We estimate internal variability
133 from a comprehensive SMILE, avoiding the stationarity assumption common in previous work, which we show is
134 violated. Then, we examine the partitioning among different sources of uncertainty (Sect. 3.2) and ~~the scale~~
135 ~~dependence of this partitioning~~ provide a novel analysis of how the three sources of variability change across the
136 full continuum of scales (Sect. 3.3) ~~to understand~~. Having Shown how the uncertainty and distribution among
137 sources differ based on scale of integration and region of interest, we analyse local patterns of uncertainty by the
138 source (Sect. 3.4). The final section explores the detectability of the model projected signal given the uncertainty
139 imposed by internal variability; We report on the scenario-dependent Time of Emergence, using a scenario specific
140 measure of internal variability in order to make useful suggestions for future observations.

143 2. Data and Methods

144 2.1 Model Data Selection

145 Here we use results from models selected from the 6th Coupled Model Intercomparison Project (CMIP6; Eyring
146 et al., 2016). Models are chosen based on availability, meaning all models that provided at least one realisation
147 for air-sea CO₂ flux (fgco2) for the CO₂ concentration driven experiments of interest. One realization of each
148 model over the historical period and three scenarios that represent the low (ssp126), mid (ssp245), and high
149 (ssp585) ranges of future atmospheric CO₂ concentrations are analysed. A total of 16 models met these criteria,
150 out of which 3 were excluded as outliers (see section S1 in the Supplements). To maintain equal sampling, only
151 one realization of each model ~~is~~was selected, except when specifically using the large ensembles to assess
152 internal variability. Finally, since the ocean component of the models may be on different grids, all model data
153 ~~are remapped to a regular one-by-one-degree grid.~~ were remapped to a regular one-by-one-degree grid and a 10
154 year running mean filter was applied to the time-series. We did not account for potential drift in the models.
155 However, the drift is known to be small in the models compared to the historical trends for CMIP5 models
156 (Hauck et al, 2020). For 11 of our CMIP6 models for which piControl runs are available, on average, the drift is
157 more than one order of magnitude smaller than the change in the model scenario with the smallest trend over the
158 21st century, on the global scale.

159

160 2.2 Sources of uncertainty

161 ~~Three sources of uncertainty are considered following the approach of HS09.~~ Total uncertainty is composed of
162 internal, model, and scenario uncertainty in equation 1, which assumes that each of these sources is independent.
163 Here, each source of uncertainty is considered as a function of time (t) and location (l) (Lovenduski et al., 2016):

164

$$165 U_T^2(t, l) = U_I^2(t, l) + U_M^2(t, l) + U_S^2(t, l) \quad (1)$$

166

167 where $U_T(t, l)$ is total uncertainty, $U_I(t, l)$ is internal variability, $U_M(t, l)$ is model uncertainty, and $U_S(t, l)$ is
168 scenario uncertainty. The fractional uncertainties for each source are calculated as $\frac{U_I^2}{U_T^2}$, $\frac{U_M^2}{U_T^2}$, and $\frac{U_S^2}{U_T^2}$ (Lovenduski et
169 al., 2016).

170

171 HS09 assume $U_I(t, l)$ to be constant in time (stationary) and use a 4th degree polynomial fit to measure internal
 172 variability as the spread over time and scenario of the residuals for each ~~models~~ model's signal relative to the fitted
 173 signal. We show in the Supplements (see section S2) that internal variability depends on time and scenario, ~~so a~~
 174 ~~better estimate~~ violating the commonly used assumption of internal variability should stationarity. Using a SMILE
 175 allows us to account for these variations: ~~without having to make any assumptions about distribution or stationarity~~
 176 of variability (Frolicher et al., 2015; Schlunegger et al., 2020). Here, we ~~quantify~~ estimate internal variability as
 177 two times the standard deviation of the annual carbon sink across ~~many~~ 50 realizations from a Single Model Initial
 178 Condition Large-ensemble based on CanESM5: (Eq. 2):

$$U_I(t, l) = 2 \sqrt{\frac{1}{N_s} \sum_{s=1}^{N_s} \text{Var}(\text{CanESM5 Large Ensemble})} \quad (2)$$

182
 183 where s indicates each scenario (N_s is the number of scenarios) and Var indicates the variance over the large
 184 ensemble of CanESM5. In the CanESM5 SMILE, each realization starts from different initial conditions which
 185 are drawn from points separated by 50 years in the piControl simulation. Thus, the spread across the realizations
 186 gives a robust estimate of the internal variability, including sampling over longer term ocean variability. ~~Internal~~
 187 ~~variability is an important component of the uncertainty that is not reducible and results from the chaotic nature of~~
 188 ~~the climate system. Further details regarding the estimation of internal variability are explained in the Supplements~~
 189 ~~(see section S2).~~ CanESM5

190
 191 Previous studies have also used SMILEs to estimate variability (Frolicher et al., 2015; Schlunegger et al., 2020),
 192 although they used either a limited ensemble size or single scenario. We show in the Supplements (Fig. S2), that a
 193 sufficiently large ensemble size is needed to capture internal variability, and that internal variability depends on the
 194 scenario. In the ideal case, if every CMIP model provided sufficiently large SMILEs for each scenario, an ensemble
 195 mean estimate of the variability could be obtained and would represent a best estimate (but still possibly biased
 196 compared to the real world). However, only a handful of CMIP6 models produced multiple ensemble members.
 197 We selected the CanESM5 SMILE as it is the only model that has a large enough ensemble over the entire timeline
 198 and set of experiments to make ~~this~~ estimate internal variability robustly and across scenarios.

199
200
201
202
203
204
205
206
207
208
209
210
211
212
213
214
215
216
217
218
219
220
221
222
223
224
225
226

The use of a single model to estimate the scale of internal variability leads to some uncertainty in our estimates, as models do not agree perfectly with each other on the variability. Nonetheless, over the historical period, variability between large ensembles from three models that have enough ensemble members is within 10%, on the global scale (Fig S3). Differences will be larger at smaller scales; however, the general patterns of the magnitude of internal variability (see Fig. S4) are in good agreement across models and are consistent with known regions of high variability in the observed ocean, validating our use of the CanESM5 SMILE

Model uncertainty is calculated by taking the variance across the forced signal of all available models for each scenario, averaging over the three scenarios, and then reporting twice the square root of the result (Eq. 3).

$$U_M(t, l) = 2 \sqrt{\frac{1}{N_s} \sum_{s=1}^{N_s} \text{Var}_m(F(m, s, t, l))} \quad (3)$$

where Var_m means the variance taken across different models for individual times and scenarios, m indicates each model, and t stands for time. $F(m, s, t, l)$ is the forced signal and can be related to each realization as follows:

$$T(m, s, t, l) = F(m, s, t, l) + R(m, s, t, l) \quad (4)$$

Where, $T(m, s, t, l)$ represents the reported output, i.e. each realization, but must be corrected for internal variability. $R(m, s, t, l)$ is the residual from the forced signal caused by internal variability. Here, the variance in the forced signal across all models is calculated by correcting the total variance across ~~each model~~ all models' one realization for the variance caused by internal variability. The corrections are done by subtracting the variance across the same number of CanESM5 ensemble members as the multi-model ensemble (13 members) from the spread variance across the one realization of ~~each~~ all of the 13 models. For this correction only, the sample sizes (13) are kept the same so that the internal variability removed from the variance across the models' first realizations is not overestimated by a well sampled 50-member ensemble (see section S3 in the Supplements).

$U_s(t, l)$ is the scenario uncertainty. Scenario uncertainty is measured as twice the standard deviation (square root of variance) across scenarios of the multi-model mean signal (Eq. 5).

227

228

$$U_S(t, l) = 2 \sqrt{\text{Var}_m \left(\frac{1}{N_m} \sum_{m=1}^{N_m} T(m, s, t, l) \right)} \quad (5)$$

229

230

231

232

233

234

235

236

237

238

239

240

241

242

243

244

245

246

247

248

249

250

251

252

253

where N_m is the number of models. The multi-model mean across the first realizations of the 13 models gives the multi-model forced response and does not require correction for internal variability as done for model uncertainty before.

We conduct analysis on three different scales: single grid point (one-degree resolution), regional, and global. When regional and global analysis is done, the dependence on location is taken away by ~~integrating and~~ averaging over that region or the whole global ocean.

2.3 Time of Emergence (TOE)

In order to know when the forced response is distinguishable from internal variability, ~~time of emergence~~ TOE is calculated following the approach of McKinley et al. (2016). The time of emergence is the first year when the multi-model mean anomaly is larger than internal variability – approximated by two times the standard deviation across the 50 member CanESM5 ensemble - for five consecutive years (the first year of this five-year period is reported as the time of emergence). The result is reported at each grid point for the 10-year running mean smoothed anomaly relative to the 1995-2015 mean (detection of a change relative to the current state of the ocean).

2.4 Scale Dependence

Finally, the scale dependence of the sources of uncertainty is measured at year 2050 using ssp245 for internal variability and model uncertainty, and using all scenarios for scenario uncertainty. The analysis is done by moving a sliding sample window of a given area across the earth, and then repeating with a larger and larger window until all scales from $<100 \text{ km}^2$ to the whole Earth are considered. ~~The~~ For each source of uncertainty and averaging scale, the average for all rectangles ~~of~~ across the globe is reported, where each rectangle contains the same ocean area ~~across the global ocean for each source of uncertainty is reported.~~

254 3. Results and Discussion

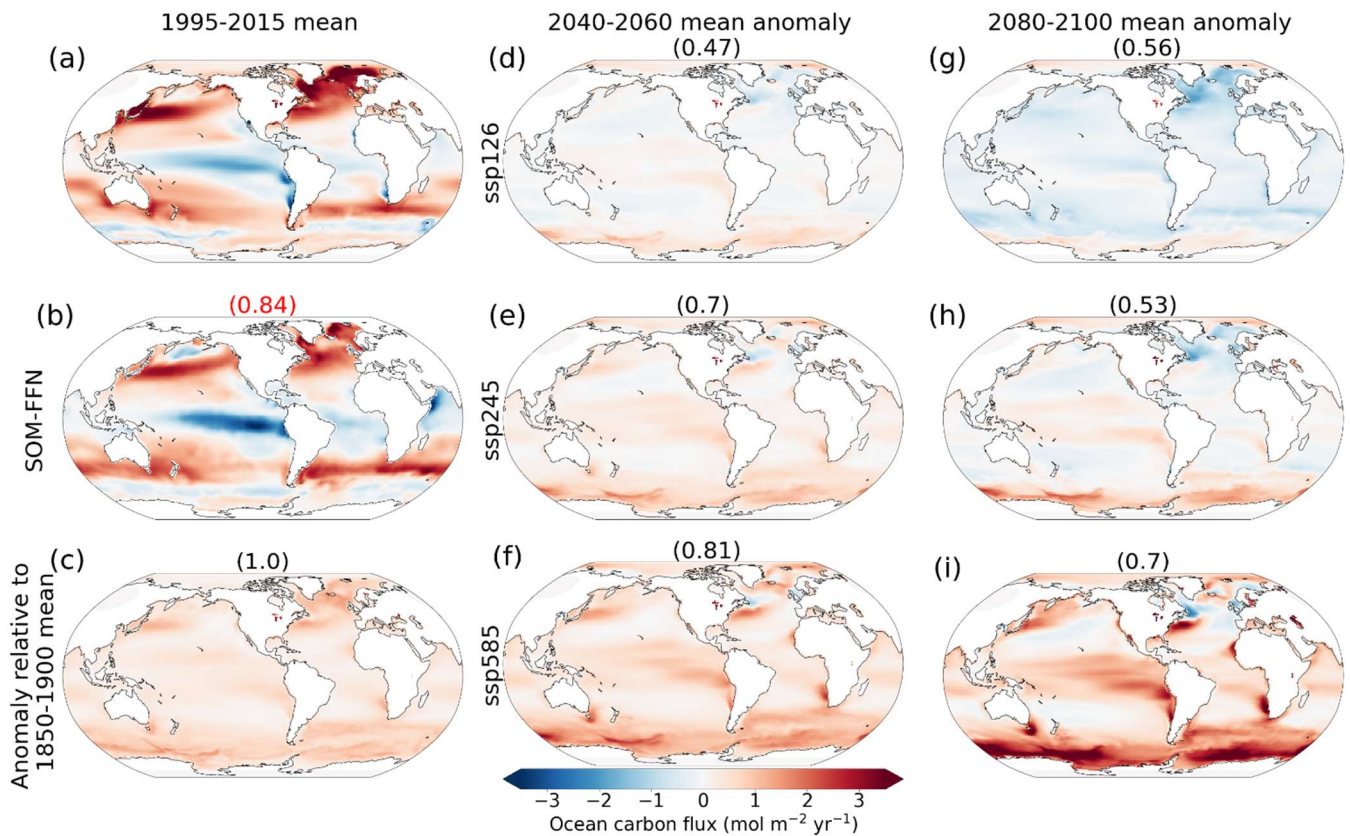
255 3.1 Global Analysis

256 The pattern of the carbon sink in the CMIP6 multi-model ensemble mean from the historical experiment over 1995-
257 2015 matches that of the Landschützer (2016) Self Organizing Map - Feed Forward Neural Network (SOM-FFN)
258 observation-based data product estimate (correlation coefficient of 0.84, compare Figs. 1a and 1b). We use the
259 multi-model mean response to external forcing as a more robust estimate of the forced climate signal than the
260 response of any single model (Tebaldi & Knutti, 2007). Unlike in ESMs, the observation-based product only
261 represents the one realization of the real world, which includes internal variation, and is therefore not directly
262 equivalent to the forced signal. However, the comparison to the 20 year mean multi-model mean still informs us
263 about the degree of agreement between the two products. When compared to the observation-based data product,
264 the CMIP6 multi-model mean shows a larger sink (positive flux) in the North Atlantic and North and North-West
265 Pacific but a smaller sink in the Southern Ocean (Fig 1a, b). Additionally, the observation-based data product shows
266 a larger source in the Equatorial Pacific and Indian Ocean than the CMIP6 multi-model ensemble.

267
268 While most of the global ocean shows a net sink relative to the pre-industrial era, the largest change takes place in
269 some highly active regions such as the subpolar North Atlantic, Southern Ocean, Eastern Equatorial Pacific, and
270 western boundary currents of the mid-latitude gyre systems in the Pacific and Atlantic Oceans (Fig. 1c). These
271 regions of largest change in the carbon sink (anthropogenic plus changes in the natural carbon sink seem to be) are
272 the regions where there is a surface-depth connectivity. We refer to these regions as “hotspots” from here on. The
273 air-sea flux of anthropogenic carbon is fundamentally limited by the rate of surface-to-depth transport (Graven et
274 al., 2012; Ridge and McKinley 2021). These results for CMIP6 models are consistent with those for CMIP5 models
275 shown by McKinley et al. (2016) and earlier studies such as Sarmiento et al. (1998). Here, we provide a new
276 metric for quantifying these highly active regions. We find that for all three scenarios and both mid-21st century
277 (2040-2060 mean) and late- 21st century (2080-2100 mean) time periods (with the exception of ssp126 late-century
278 where strong mitigation of anthropogenic CO₂ emissions results in broad patterns of negative anomalies),
279 approximately 70% of the changes in the sink relative to the preindustrial area takes place in less than 40% of the
280 global ocean (see Supplement Fig. S7 and section S5).

281
282 The regions of largest future carbon uptake, relative to the 1995-2015 mean, are within the same highly active
283 regions responsible for most of the uptake over the historical period. The correlation coefficients on at the top of

284 each panel in Fig. 1 (except 1b) represent the pattern correlation between future absolute anomalies, relative to
 285 1995-2015, and anomalies in 1995-2015, relative to the pre-industrial era. The high correlations indicate that
 286 regions that have been most active in carbon sequestration since the pre-industrial era are the same regions that will
 287 continue to change most into the future, particularly with larger increases in atmospheric CO₂ (ssp585). Our results
 288 support the findings of Wang et al. (2016) who showed that projected future air-sea CO₂ fluxes are strongly
 289 associated with simulated historical air-sea CO₂ fluxes. This confirms that the historical state is a good predictor
 290 for the future state (Wang et al., 2016) not only in terms of magnitudes of the sink, but also in the spatial pattern.
 291
 292
 293



294
 295 **Figure 1-** CMIP6 multi-model mean maps of carbon sink and sink anomalies using one realization of each model. Columns
 296 represent different time periods, being the recent time (1995-2015 mean), mid-century (2040-2060 mean), and late-century
 297 (2080-2100 mean). Note: the sink is positive into the ocean. The first column shows (a) the carbon-sinkCMIP6 ensemble
 298 mean air-sea CO₂ flux over 1995-2015, (b) Landschützer et al. (2016) SOM- FFN product, and (c) the CMIP6 ensemble

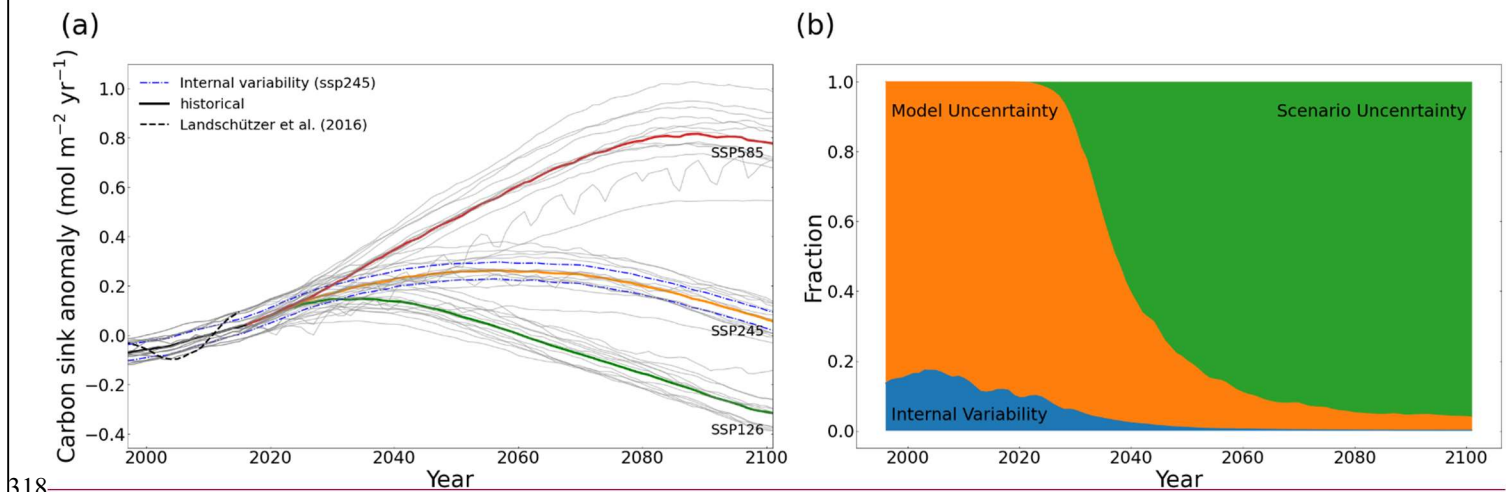
299 mean flux anomaly relative to the 1850-1900 mean. Other panels are anomalies relative to the 1995-2015 multi-model mean
 300 (panel a). Panels d through i show different scenarios. Numbers above each map are correlation coefficients between the
 301 absolute value of the change relative to 1995-2015 with the 1995-2015 anomaly map relative to the pre-industrial era in
 302 panel c, except the red number at the top of panel b that is the correlation coefficient with this panel and panel a.

303

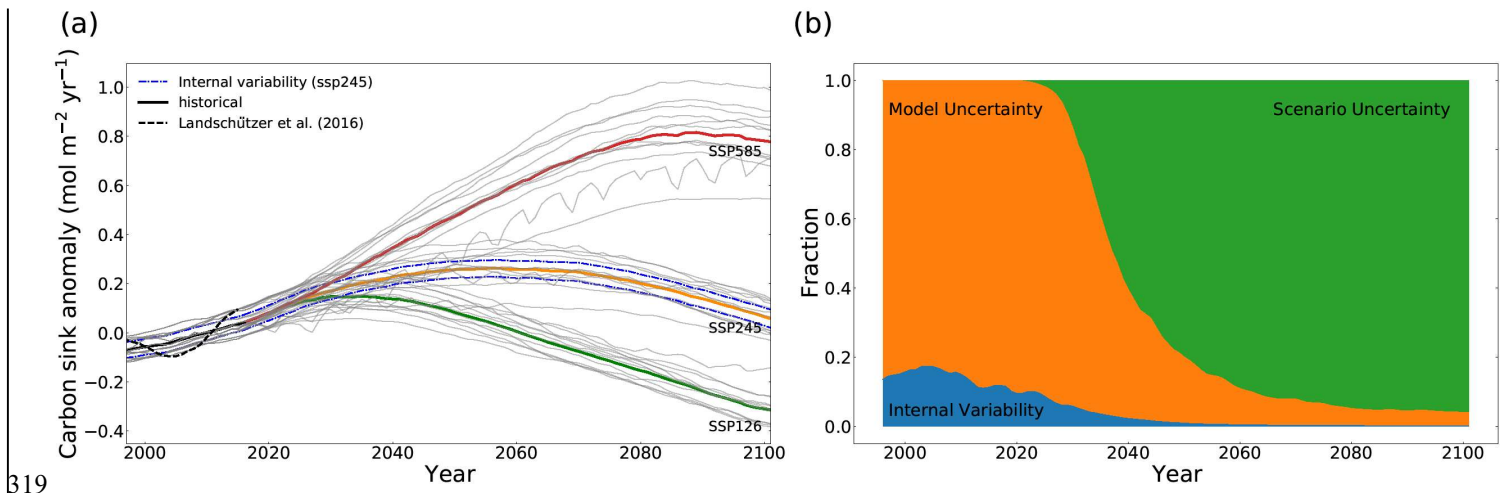
304 The multi-model mean sink anomalies for two future periods, 2040-2060 and 2080-2100, show how the sink is
 305 projected to evolve, relative to 1995-2015, according to time and choice of emission scenario (Fig. 1d-i). The
 306 regional patterns show mostly positive anomalies at mid-century: with largest changes in the higher emission
 307 scenarios (ssp585). Towards the end of the century, however, broader patterns of negative anomalies are expected
 308 in ssp126, as emissions turn negative in the late-century in this scenario. The largest absolute values of anomalies
 309 are still within the same highly active regions discussed before with surface-depth connectivity regardless of it
 310 being positive or negative. The late-century anomalies are predominantly positive in ssp585 which corresponds to
 311 the highest emission scenario; (continuing to grow larger compared to the mid-century), while ssp245 is somewhere
 312 in between, with regions of positive and negative anomalies. Under ssp245, as CO₂ emissions decrease and
 313 atmospheric CO₂ start to level off, the intensity of uptake decreases in the midlatitude western boundary currents
 314 and subpolar North Atlantic in the late-century, and anomalies in the Eastern Equatorial Pacific also decrease,
 315 compared to the mid-century. The globally integrated ocean carbon uptake rates are summarized in Table 1.

316

317



318



319
 320 **Figure 2-** (a) Thick lines are multi-model means of the global mean ocean carbon sink anomaly timeseries relative to 1995-
 321 2015. Individual models ~~averaged for the means~~ are plotted as thin grey lines in the background. The black dashed line
 322 shows the Landschützer et al. (2016) SOM-FFN product. Both models and SOM-FFN timeseries are smoothed with a 10-
 323 year running mean. The blue dashed lines show internal variability for ssp245. (b) Timeseries showing the breakdown of
 324 uncertainty to different sources with time for the global ocean carbon sink anomaly. The internal and model uncertainty are
 325 averaged for different scenarios.

326
 327
 328
 329
 330
 331
 332
 333
 334
 335
 336
 337
 338
 339
 340

| | Scenario | 1995-2020 | 2020-2040 | 2040-2060 | 2060-2080 | 2080-2100 |
|---|----------------|------------------------|-----------------------|------------------------|---------------------------|-------------------------|
| Anomaly (range) | ssp126 | | 0.13 (0.05 – 0.21) | 0.07 (-0.02 – 0.16) | -0.08 (-0.14 - -0.01) | -0.24 (-0.3 - -0.12) |
| | ssp245 | 0.00 (-0.06 – 0.06) | 0.17 (0.08 – 0.24) | 0.25 (0.11 – 0.36) | 0.23 (0.09 – 0.33) | 0.13 (0.02 – 0.21) |
| | ssp585 | | 0.22 (0.11 - 0.30) | 0.49 (0.29 – 0.62) | 0.71 (0.45 – 0.90) | 0.80 (0.54 – 1.00) |
| Internal (model) Uncertainty | ssp126 | | 0.033 (0.11) | 0.034 (0.11) | 0.035 (0.10) | 0.036 (0.11) |
| | ssp245 | 0.032 (0.08) | 0.032 (0.11) | 0.034 (0.14) | 0.037 (0.14) | 0.036 (0.12) |
| | ssp585 | | 0.033 (0.13) | 0.037 (0.2) | 0.045 (0.26) | 0.043 (0.27) |
| | Average | 0.032 (0.08) | 0.033 (0.12) | 0.035 (0.16) | 0.039 (0.18) | 0.038 (0.18) |

341

342

343

344

345

346

347

348

349

350

351

352

353

354

355

Table 1- CMIP6 multi-model mean globally averaged carbon sink anomalies (with ranges within the 20-yr period in parentheses) relative to the 1995-2015 mean (in mol-C m⁻² yr⁻¹) and ~~Internal~~internal variability from CanESM5 (with model uncertainty in parentheses) for the globally averaged ocean carbon sink anomalies for the three scenarios and the average values across scenarios.

The trends in the global mean ocean carbon sink anomalies over 1995-2015 are statistically consistent between the CMIP6 multi-model ensemble mean and the Landschützer et al. (2016) observation-based data product (Fig. 2-a), based on the test from Santer et al. (2008)-; see Supplements section S5). However, the SOM-FFN based time-series shows a larger multi-decadal variability (variations in the 10-year running mean timeseries on top of the trend) than seen in individual model realizations, and is larger than the range of internal variability estimated from the CanESM5 SMILE. The difference could be due to either overestimation of internal variability by the SOM-FFN method, or underestimation of the internal variability ~~in~~from the ~~models~~ESMs. Given that on regional scales the SOM-FFN data is within the range of internal variability projected by the CMIP6 large-ensemble of CanESM5

356 (see Sect. 3.3), and that there are significant gaps in the spatial and temporal sampling that underlies the
357 Landschützer et al. (2016) estimate, it seems plausible that the discrepancy is largely due to overestimation of
358 internal variability on the global scale by the SOM-FFN technique. This is consistent with the findings of Gloege
359 et al. (2021), which showed that, globally, the magnitude of decadal variability is overestimated by 21% by the
360 SOM-FFN technique, attributed to the amount of data filling.

361

362 On the global scale, model uncertainty is the dominant source of uncertainty in the historical period, but scenario
363 uncertainty comes to dominate later (Fig. 2b). Over the 1995-2020 period, model uncertainty explains around 85%
364 of the total uncertainty. Scenario uncertainty becomes the dominant source after 2040, explaining almost 40% of
365 the total uncertainty at that time and more than 90% by the end of the century. Internal variability explains 15% at
366 the start of the century but only around 1% by the end. It is worth mentioning that the decreased share of
367 uncertainty associated with model and internal variability do not mean that model or internal variability decrease
368 in an absolute sense; rather, their importance relative to scenario uncertainty declines. Internal
369 regarding the importance of model and scenario uncertainties for multidecadal projections, and dominance of
370 scenario uncertainty with time agree with previous studies using CMIP5 models (Lovenduski et al., 2016;
371 Schlunegger et al., 2020).

372

373 Absolute internal and model uncertainty of the global carbon sink change with time, based on the scenario (Table
374 2); high, Fig. S3). High emission scenarios such as ssp585 show a larger change for both internal and model
375 uncertainty; where the forcing is stronger (Fig. S3). When averaged for the three scenarios, a constant absolute
376 increase in the magnitudes of both model and internal variability is seen through the century until 2080-2100 when
377 the values either do not change or decrease slightly (Table 1). Model uncertainty more than doubles towards the
378 end of the century compared to 1995-2015 on average for different scenarios. This is consistent with Lovenduski
379 et al. (2016) who argues that the increase is due to difference in climate sensitivities between models that manifest
380 more strongly with time (and hence cumulative emissions). Additionally, the dependence of internal variability on
381 the scenario is an interesting result. Future SMILEs from multiple models will allow evaluation of the degree of
382 dependence and the driving mechanisms of such changes with time based on the forcing (scenario). Our result of
383 internal variability dependence on scenario implies that the time of emergence of a signal out of internal variability
384 will be affected by changes in the internal variability under different future forcing scenarios – which we return to
385 in Section 3.4.

386

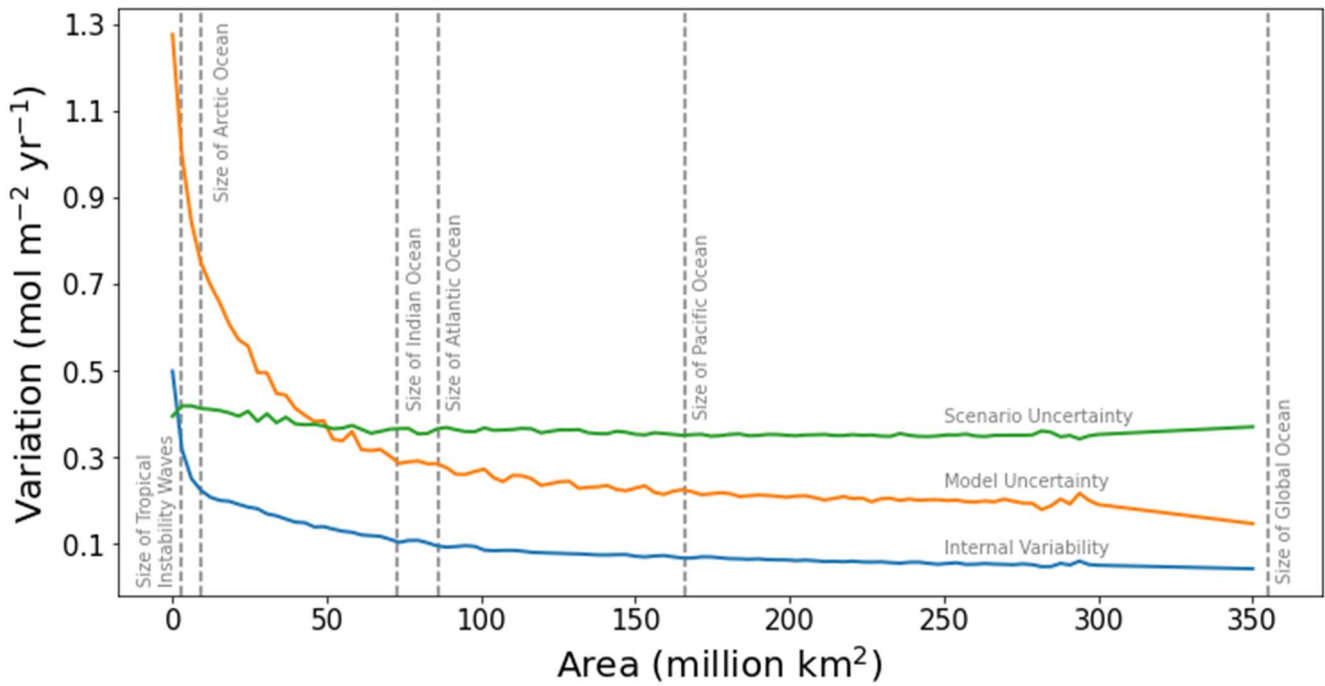
387

388 3.2 Dependence of the sources of uncertainty on spatial scale

389 It is generally accepted that uncertainty and, most importantly, internal variability grow larger as the averaging
390 (integration) scale gets finer, because on larger scales the variability is averaged out. ~~Lovenduski et al. (2016)~~
391 ~~showed this scale dependence by comparing an area covering the California Current System with the global ocean.~~
392 ~~Here, we provide a~~Here, we provide a novel and continuous view of change in variability across scales from the
393 global to grid scale, by measuring how variability changes relative to scale on average (Fig. 3). At the global scale,
394 the dominant source of uncertainty is scenario uncertainty, followed by model and internal variability respectively,
395 consistent with Fig. 2b. However, as the averaging (integration) scale gets finer, model and internal variability
396 grow rapidly, while scenario uncertainty only grows slightly on average (over all regions of this size). At an
397 averaging (integration) scale with an area finer than 75 million km² (on average around the globe), model
398 uncertainty becomes the dominant source of uncertainty, and at a scale finer than 3 million km², internal variability
399 becomes larger than scenario uncertainty. ~~However, while this holds true on average over the globe, scale~~
400 ~~dependence can vary in its nature depending on the particular region being sampled.~~The idea of scale dependence
401 of these uncertainties was tested in Lovenduski et al. (2016) by comparing an area covering the California Current
402 System with the global ocean. Here, we provide a novel analysis on a continuum of scales covering global to
403 regional to local scales. While the results here hold true on average over the globe, scale dependence is partially
404 controlled by the particular region being sampled. Finally, while our estimates of the magnitudes of sources of
405 uncertainty and the cross over points at which the dominance of internal variability over model uncertainty and
406 model uncertainty over scenario uncertainty takes place, depend on the choice of ESMs and the method for
407 calculation of internal variability, the general patterns are unlikely to be model dependent.

408

409



410

411 **Figure 3-** Sources of uncertainty versus area of averaging. Internal variability is based on ssp245 year 2050 of all CanESM5
 412 members. Scenario uncertainty is based on all scenarios of the 13 models at year 2050 and model uncertainty is the corrected
 413 standard deviation of our 13 models at year 2050 of ssp245. The values of uncertainties are averaged over all different
 414 rectangular areas of each size that can scan the globe. Dashed lines indicate the size of the averaging window and not a
 415 specific location.

416

417

418 3.3 Regional Analysis

419 ~~The~~ We further expand on the findings of ~~our analysis of the globally-averaged-scale dependence analysis were~~
 420 ~~tested of uncertainty averaged over the globe~~ by repeating the uncertainty breakdown for two specific regions: one
 421 between 2040°- 60° N in the ~~North East~~ Northeast Pacific (NE Pacific) between 130°- 160° W and one in the ~~North~~
 422 ~~West~~ Northwest Atlantic (NW Atlantic) between 40°- 70° W at the same latitude. ~~We chose these regions, first, to~~
 423 ~~be of the similar size, and second to represent very different carbon dynamics.~~ The NW Atlantic region represents
 424 a ~~hotspot highly active region~~ while the NE Pacific region is more typical of quiescent ocean regions. ~~By quiescent~~
 425 ~~ocean regions we refer to regions, where strong stratification limits the vertical transport of carbon by isolating the~~
 426 ~~surface the flux anomalies are relatively small.~~

427

428 The variation across scenarios is at all times smaller than internal variability in the NE Pacific (Fig. 4a). This
429 suggests both that it will be difficult to robustly detect any human induced changes in observations of the NEP
430 carbon sink, and that potential future differences relating to choice of mitigation scenarios will not be readily
431 apparent in the NE Pacific carbon flux. This is true even for the high emission scenarios, because the anomalies
432 are small regardless of scenario (Table 2). We speculate that in the absence of mechanisms providing a pathway
433 to the depth where significant CO₂ accumulation occurs, the surface pCO₂ trend will follow that of the
434 atmosphere closely, causing ΔpCO₂ and therefore air-sea carbon flux to remain fairly constant for all scenarios. In
435 the NW Atlantic however, the deviation across scenarios becomes larger than the internal variability in the early
436 2060s (Fig. 4c). The response of the region to climate change is dependent on the scenario (Table 2), or, in other
437 words, the amount of carbon dioxide in the atmosphere. This is because the NW Atlantic is a hotspot highly active
438 region where the air-sea flux actively responds to the atmospheric CO₂ concentration. The connection to depth
439 allows for surface water to be replaced with water masses whose pCO₂ trend lags behind that of atmosphere. The
440 trend of the CMIP6 multi-model time-series over the historical period is statistically consistent (~~Santer et al.,~~
441 2008See Supplements section S5) with that of the observation-based SOM-FFN product, and the multi-decadal
442 variability is within the range of internal variability measured by the CanESM5 large-ensemble in both regions.
443 We note that both of these regions are relatively well sampled, which may lead to more robust estimates of multi-
444 decadal variability in the Landschützer et al. (2016) dataset, and better agreement with the models than seen at
445 the global scale.

446

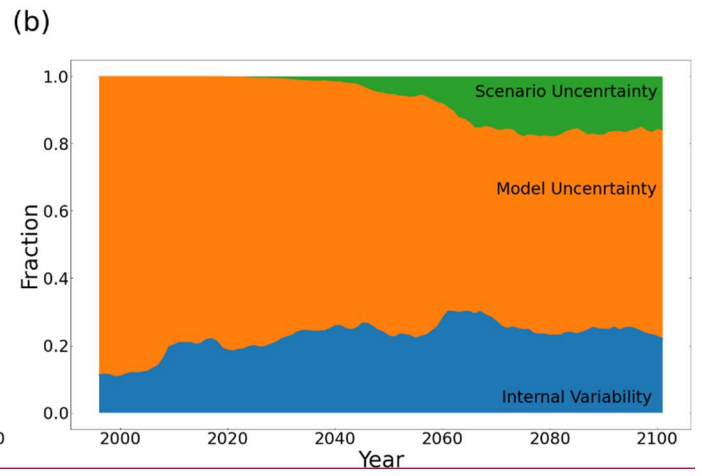
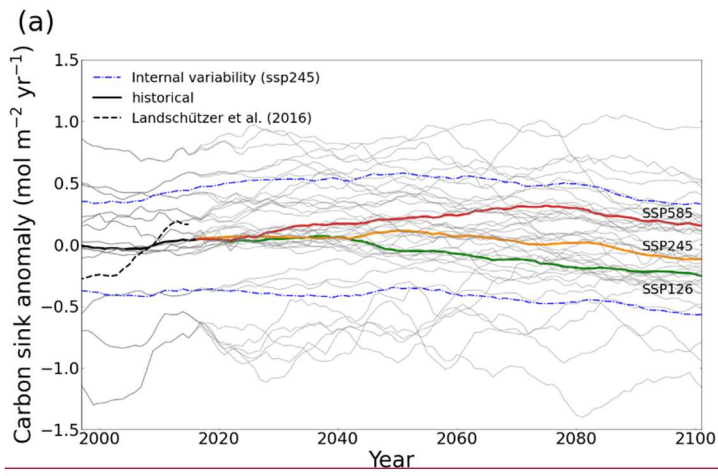
447 Fractional estimates of each source of uncertainty vary with time and have different patterns for these two regions.
448 Internal variability and model uncertainty in the NE Pacific and NW Atlantic are larger by an order of magnitude
449 than at the global scale (Table 2). A lesser importance for scenario uncertainty and greater importance for internal
450 and model uncertainty is apparent in both regions compared to the global scale, in agreement with Schlunegger et
451 al. (2020). Over the period 1995-2020, model uncertainty is the dominant source of uncertainty in both the NE
452 Pacific and NW Atlantic (80-90%), while the remainder is internal variability (Fig. 4bd). Internal variability
453 explains around 25-30% of the total uncertainty in the NE Pacific throughout the century. In the NW Atlantic
454 however, its share drops to 15% by the end of the century. The share attributable to internal variability is much
455 larger during the 21st century in both regions compared to the global scale. Internal variability is larger in the NW
456 Atlantic in an absolute sense (Table 2), but its share of the total uncertainty is larger in NE Pacific (Fig. 4b). The
457 large share of internal variability in NW Pacific indicates the need for sustained observations in the region. Overall,
458 internal variability averaged over the scenarios shows a small increase, but no clear trend in time in both regions

459 until the 2080-2100 period where it decreases, consistent with the global estimates. ~~The dependence of internal~~
460 ~~variability on the scenario is an interesting result which requires further evaluations to understand the degree of~~
461 ~~dependence and the driving mechanisms of such changes with time based on scenario. (Table 2).~~ We showed earlier
462 that in the NE Pacific scenarios do not differ ~~much as~~ because the region is ~~not a hotspot~~ highly active region (Fig.
463 S7) - scenario uncertainty explains less than 20% of the total uncertainty at the end of the century in the NE Pacific.
464 In the NW Atlantic, scenario uncertainty grows larger with time, becoming 45-50% of total uncertainty by the end
465 of the century. In both regions, model uncertainty is the dominant source of uncertainty in all years.

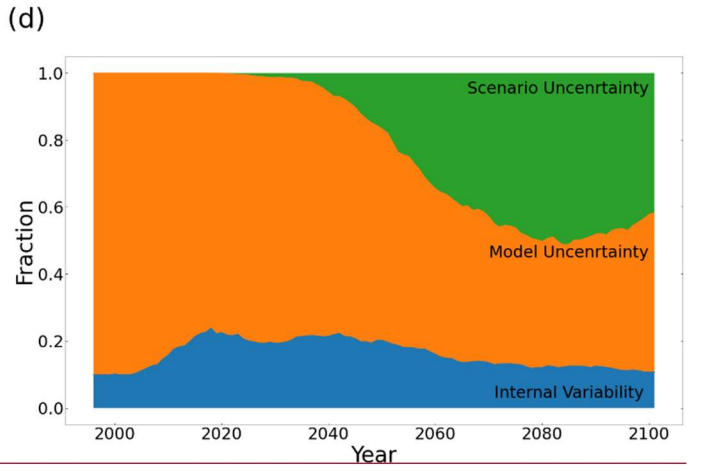
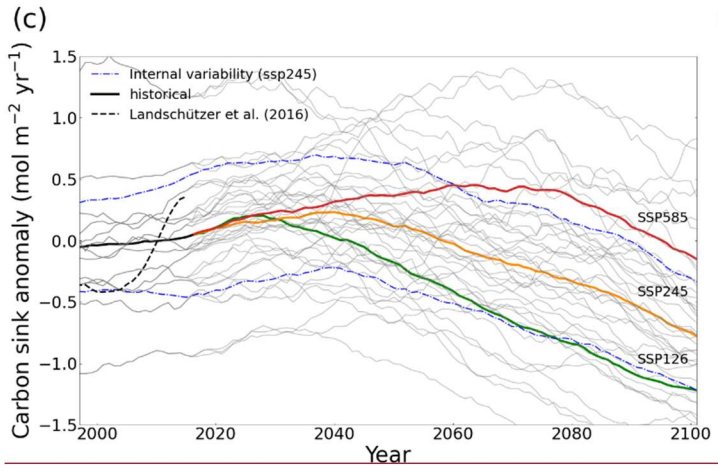
466
467 Our regional analysis confirms that while uncertainty and its distribution among sources depends on the spatial
468 scale of integration, the specific location also matters (Lovenduski et al, 2016; Schlunegger et al., 2020).
469 Schlunegger et al., (2020) tested this idea for 10 ocean basins but with different sizes (see their Figure 9). We
470 focused on keeping the sizes similar and analyse a highly active region versus a more quiescent ocean region. The
471 key message here that there is an association with the importance as well as the magnitude of sources of uncertainty
472 with how active the region is in regards to the carbon sink is not sensitive to the use of CanESM5 for estimation of
473 internal variability. Local patterns of uncertainty broken down by source are thus needed to clarify changes based
474 on location.

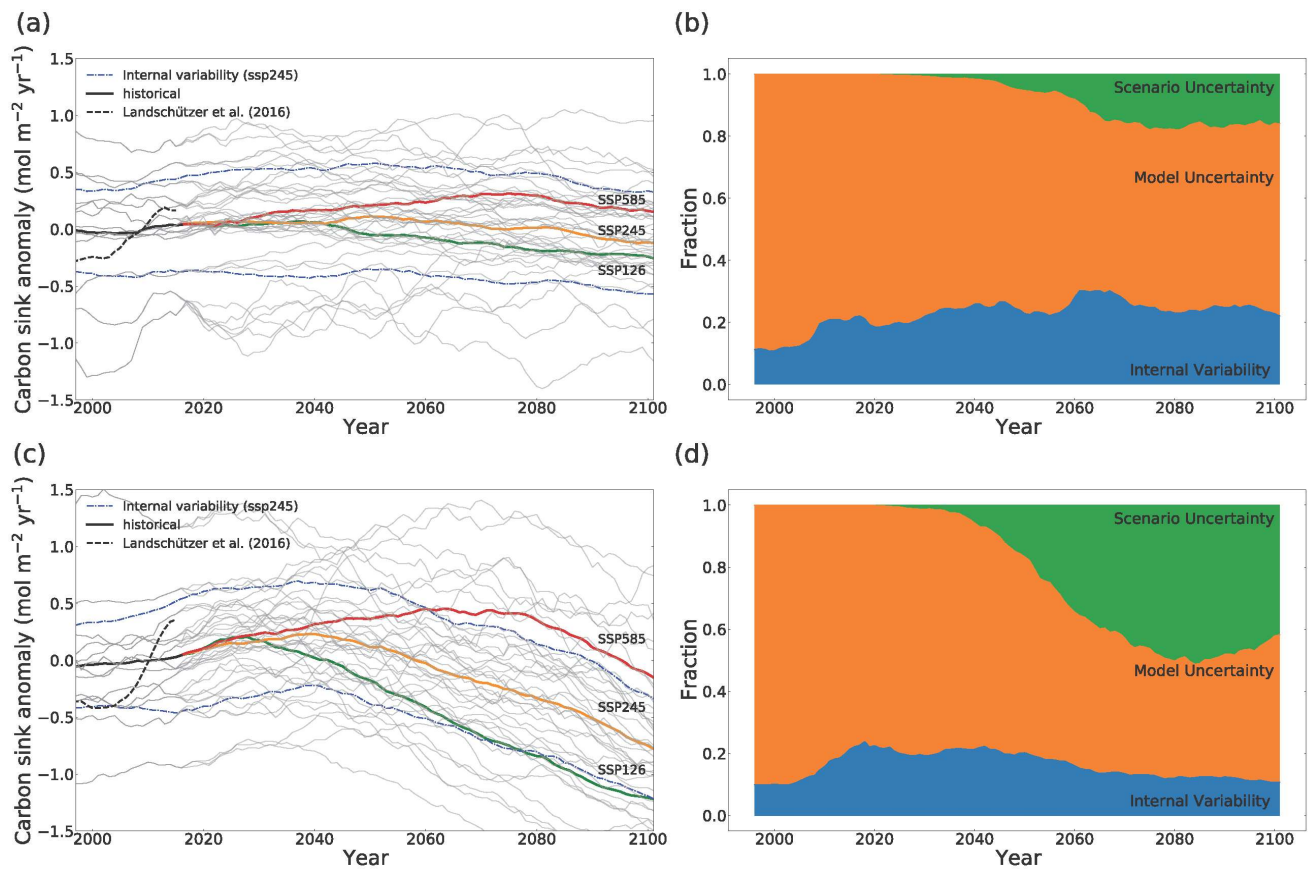
475
476
477
478
479
480
481
482
483
484
485
486
487
488

489



490





491

492 **Figure 4-** (a), (c) Thick lines are multi-model mean timeseries of anomalies relative to the 1995-2015 mean. All model time-
 493 series averaged for the means are plotted in grey lines in the background. The black dashed line shows the Landschützer et al. (2016)
 494 SOM-FFN product. The blue dashed line shows the internal variability measured as two times the standard
 495 deviation across all 50 members of CanESM5 only for ssp245 here. (b), (d) time-series showing the breakdown of
 496 uncertainty to different sources with time. The internal and model uncertainty are averaged for different scenarios. (a), (b)
 497 NE Pacific (40-60 °N, 130-160 °W). (c), (d) NW Atlantic (40 - 60 °N, 40-70 °W)

498

499

500

501

502

503

504

| | | Scenario | 1995-2020 | 2020-2040 | 2040-2060 | 2060-2080 | 2080-2100 |
|------------------------|---|---------------|------------------------|------------------------|-------------------------|---------------------------|--------------------------|
| NE Pacific | Anomaly (range) | ssp126 | | 0.05 (-0.91 – 0.86) | 0.03 (-0.86 – 0.62) | -0.13 (-1.1 – 0.58) | -0.21 (-1.18 - 0.60) |
| | | ssp245 | 0.00 (-0.98 – 0.76) | 0.06 (-0.86 – 0.83) | 0.09 (-0.74 – 0.81) | 0.03 (-0.65 – 0.60) | 0.06 (-0.70 – 0.53) |
| | | ssp585 | | 0.11 (-0.73 - 0.79) | 0.21 (-0.61 – 0.86) | 0.29 (0.22 – 0.94) | 0.2 (-0.25 – 0.98) |
| | Internal (model) Uncertainty | ssp126 | | | 0.47 (0.87) | 0.43 (0.74) | 0.40 (0.81) |
| ssp245 | | 0.39 (0.90) | | 0.46 (0.87) | 0.47 (0.81) | 0.48 (0.64) | 0.45 (0.53) |
| ssp585 | | | | 0.45 (0.81) | 0.47 (0.745) | 0.58 (0.55) | 0.44 (0.57) |
| Average | | 0.39 (0.90) | | 0.46 (0.86) | 0.46 (0.77) | 0.47 (0.70) | 0.43(0.67) |
| NW Atlantic | Anomaly (range) | ssp126 | | 0.13 (-0.77 – 1.21) | -0.20 (-1.03 – 0.56) | -0.66 (-1.45 – -0.11) | -1.00 (-1.80 - -0.56) |
| | | ssp245 | 0.00 (-0.97 – 1.31) | 0.18 (-0.78 – 1.23) | 0.10 (-0.68 – 0.80) | -0.20 (-0.97 – 0.50) | -0.54 (-1.22 – 0.07) |
| | | ssp585 | | 0.23 (-0.70 – 1.20) | 0.38 (-0.41 – 1.12) | 0.41 (-0.27 – 1.29) | 0.10 (-0.70 – 0.96) |
| | Internal (model) Uncertainty | ssp126 | | | 0.47 (0.91) | 0.47 (0.79) | 0.46 (0.78) |
| ssp245 | | 0.43 (1.02) | | 0.47 (0.96) | 0.49 (0.82) | 0.49 (0.80) | 0.47 (0.79) |
| ssp585 | | | | 0.50 (0.90) | 0.51 (0.94) | 0.52 (1.00) | 0.53 (1.00) |
| Average | | 0.43 (1.02) | | 0.48 (0.93) | 0.49 (0.87) | 0.49 (0.88) | 0.48 (0.88) |

506 **Table 2-** CMIP6 multi-model mean sink anomalies (with ranges in parentheses) relative to 1995-2015 mean (in mol-C m⁻²
507 yr⁻¹) and internal variability (with model uncertainty in parentheses) for the three scenarios and their average values in NE
508 Pacific and NW Atlantic.

509

510 ~~The regional analysis shows that while uncertainty and its distribution among sources depends on the spatial scale~~
511 ~~of integration, the specific location also matters. Regional patterns of uncertainty broken down by the source are~~
512 ~~needed to clarify changes based on location.~~ Consistent with the sink anomaly maps (Fig. 1), the regions that show
513 highest uncertainty for any of the sources in the future, are the same regions that show the largest uncertainties in
514 the historical period (Fig. 5). More importantly, the regions of largest future uptake uncertainty are highly correlated
515 with the historical regions of largest uptake, as shown by the pattern correlation coefficients above each panel. This
516 is a highly significant finding, because it suggests that knowledge of the regions of modern day surface carbon flux
517 anomaly provides us with information about regions of future uptake uncertainty.

518

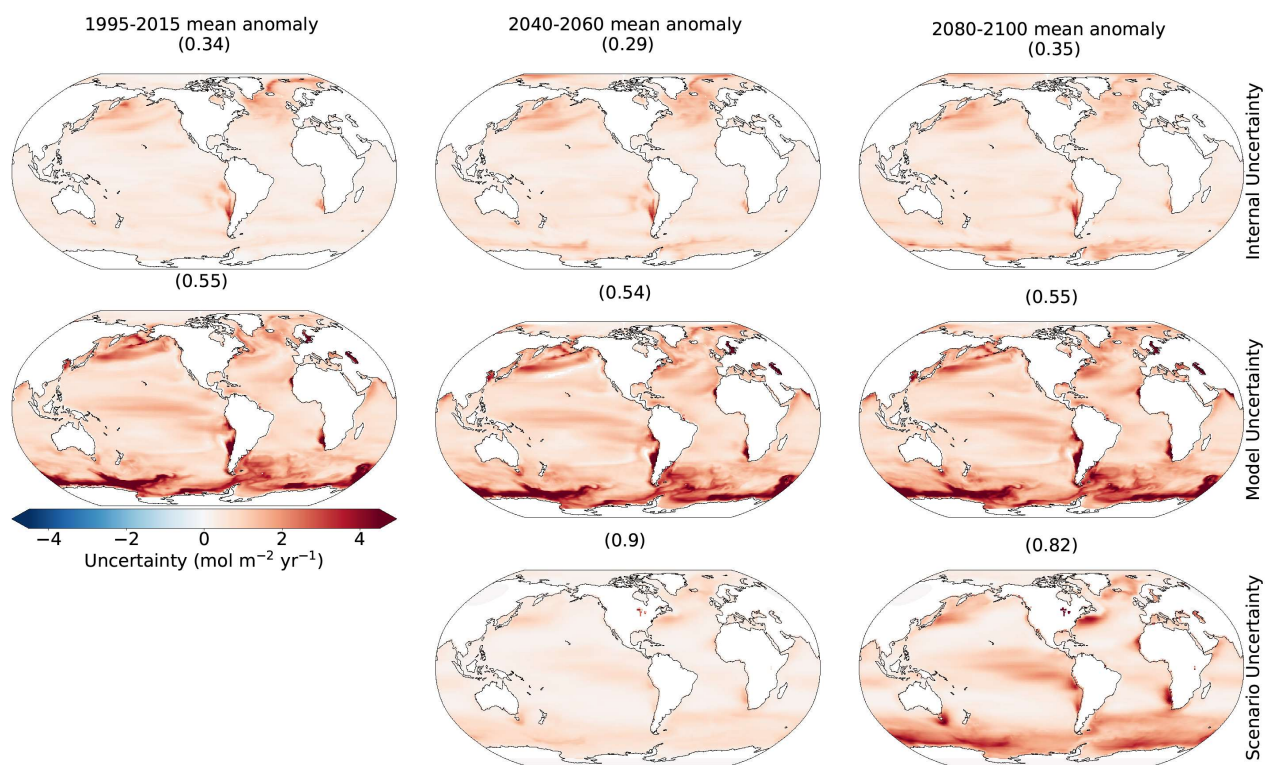
519 ~~The regions of high internal~~Internal variability (~~from CanESM5 is most dominant in mid-latitude eastern~~
520 ~~boundary upwelling regions, and their extensions, in the North Atlantic, in the western boundary currents of the~~
521 ~~Gulf Stream and Kuroshio, and their extensions, and in the Southern Ocean)~~ (Fig. 5). There is wide agreement
522 between different models and estimation methods in regions of largest internal variability (Fig. S4). The regions
523 of large internal variability are mostly within hotspots but are not confined to them and do not include all of
524 them. This lack of correspondence explains why thecorrelated with the same highly active regions for the sink
525 anomalies discussed earlier (Fig 1c). However, correlation coefficients are not high for between internal
526 variability and historical uptake are lower than those seen for scenario and model uncertainty. An increase in
527 internal variability with time is seen mostly in ~~regions such as~~ the Southern Ocean, the Arctic Ocean, and
528 boundaries of the gyre systems, while the rest of the ocean does not show a clear change. The maps in Figure 5
529 are averaged over the three scenarios, which masks the changes to some extent. However, we show in the
530 Supplements (see section S2) that changes in the globally averaged internal variability with time are different for
531 different scenarios.

532 Model uncertainty is consistently highest in the ~~hotspot~~highly active regions, (Figure S7), leading to
533 ~~stronger~~strong correlation with the anomaly maps of Fig. ~~1e, 1c~~. In these regions, ocean circulation impacts
534 surface pCO₂ through advection and water mass transformation regionally (Bopp et al., 2015; Toyama et al.,

535 2017) and models have substantial differences in ocean circulation. Ridge and McKinley (2021) suggest that
536 while global surface carbon fluxes and carbon storage are largely similar across ESMs over the historical period,
537 consistent with the external forcing from atmospheric pCO₂ growth being the main driver of the historical sink
538 (McKinley et al., 2020), uncertainties in ocean circulation may become important in the future under a changing
539 trajectory of atmospheric boundary conditions. The model uncertainty is largest in the Southern Ocean, where
540 consistent with CMIP5 models (Frölicher et al., 2015). Here, mode and intermediate waters are formed, and the
541 complex time-evolving nature of the sink varies on all time_scales (Gruber et al. 2019). Frölicher et al. (2015)
542 note the largest disagreement in ocean carbon uptake between models is in the Southern Ocean because the exact
543 processes governing heat and carbon uptake remain poorly understood. The importance of model uncertainty in
544 the Southern Ocean provides a clear focal point for modelling centres to concentrate their efforts in
545 reducing projection uncertainty. Atmospheric teleconnections might play an important role in generating the
546 highly variable Southern Ocean carbon sink on decadal scales, and these are poorly constrained and represented
547 by models (Gruber et al. 2019).

548
549 Scenario uncertainty exhibits the largest change with time. This is by construction, ~~meaning that as the~~ scenarios
550 ~~are designed to~~ deviate from each other as with time goes forward to represent a range of pathways for future
551 socio-economic possibilities in order to assess the long-term impacts of short-term decisions (Riahi et al., 2017).
552 Importantly, the correlation coefficients are highest between scenario uncertainty and the current sink regions,
553 indicating that the ~~hotspots~~ same highly active regions are the regions that show the largest divergence among
554 scenarios, and that the sink in most other regions does not respond as strongly to scenario differences. We
555 showed an example of this earlier, where the timeseries of the multi-model signals for the three scenarios did not
556 emerge out of internal variability in the NE Pacific by 2100, whereas they did for the ~~hotspot~~ highly active
557 region of the NW Atlantic. This shows that, with pCO₂ differences across the air-sea interface being the main
558 driver of the sink (Fay & McKinley, 2013; Landschützer et al., 2015; Lovenduski et al., 2007; McKinley et al,
559 2020; McKinley et al., 2017), the sink in these active ~~hotspot~~ regions, the sink evolves according to atmospheric
560 the atmospheric CO₂ concentration ~~via~~ changes because ocean processes ~~that~~ associated with surface-depth
561 connectivity constantly keep the surface ocean \ominus pCO₂ out of equilibrium with the atmosphere. In other words,
562 the surface water in these regions are constantly renewed, mostly through advection and water mass formation,
563 with water masses whose pCO₂ has not increased at the same rate as the atmosphere. Elsewhere, these conditions
564 do not hold true and water at the surface equilibrates with the atmosphere on shorter time scales, decreasing the

565 sensitivity to the projection scenario. These uncertainties are central to the ability to detect human induced trends
 566 in observations of the surface ocean carbon flux as well as to assess mitigations or make societal decisions, to
 567 which we now turn.
 568



569
 570 **Figure 5-** Sources of uncertainty averaged over the 20 year mean periods. The rows represent different sources as
 571 explained in the methods section at each grid cell. Columns represent different times: the recent (1995-2015), mid-
 572 century (2040-2060), and late-century (2080-2100) anomalies relative to the 1995-2015 mean. The numbers are
 573 correlation coefficients of each map with the 1995-2015 mean anomaly relative to the 1850-1900 mean (Fig. 1c).

574
 575 3.4 Detectability

576 Detectability refers to the ability to robustly identify a forced signal, above and beyond the noise induced by internal
 577 climate variability. Understanding Previous studies have largely presented a single time of emergence (Lovenduski
 578 et al. 2016, Schlunegger et al., 2019, McKinley et al., 2016). However, understanding the regional differences,

579 timescales, and scenario dependence in the detectability of human induced trends in the ocean surface carbon flux
580 is important for informing observational strategies that aim to measure these changes.
581

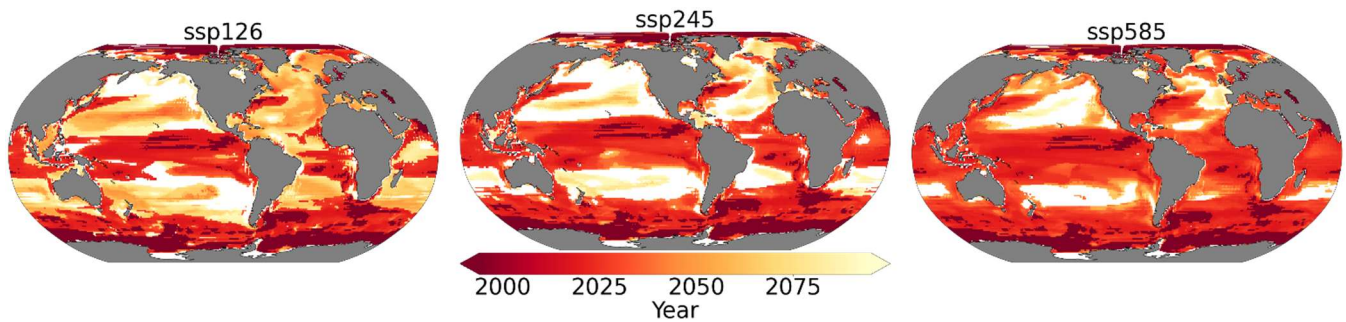
582 We measure the detectability of the CMIP6 multi-model ensemble mean ocean surface carbon flux anomaly using
583 the time of emergence at each grid point. We use this finest scale as it is the most applicable to observational
584 communities for sampling. The time of emergence is defined as the point at which the forced signal, given by the
585 multi-model ensemble mean flux anomaly, relative to 1995-2015, emerges from internal variability, given by the
586 CanESM5 SMILE.

587

588 The signal in human induced surface ocean carbon flux emerges beyond the internal variability earlier in the
589 ~~hotspot~~highly active regions than anywhere else. This is evident in the Equatorial Pacific, Southern Ocean, the
590 western boundary currents of the gyre systems, and their extensions (Fig. 6). ~~The fixed inactive Ocean~~ regions, such
591 as the centres of the mid-latitude gyre systems and the NE Pacific, show late emergence times and, in some cases,
592 no detectability of the signal in any of the scenarios by 2100. Convergent large-scale circulation and strong
593 stratification in these regions isolates the surface from the deep ocean reducing their capacity to hold large amounts
594 of carbon (McKinley et al., 2016). An absence of mechanisms constantly drawing surface ocean CO₂ out of
595 equilibrium with atmospheric CO₂ lets the surface water equilibrate with and adjust to the atmosphere on short time
596 scales. Significant changes thus do not take place in the sink as the atmospheric CO₂ levels change and scenario
597 uncertainty is lowest in the same regions (see Fig. 4). This is consistent with the results from Sect. 3.3, in which
598 we showed that internal variability is a significant source throughout the century in the NE Pacific, with scenarios
599 never emerging out of the range of internal variability (Fig. ~~4a,b~~). ~~This result argues for focusing observational~~
600 ~~efforts on the hotspot~~4a, b). Our results for the broad patterns in the multi-model mean TOE are largely consistent
601 with previous studies, suggesting they are robust and insensitive to for the method of estimating internal variability.
602 These include studies from CMIP5 models such as McKinley et al., (2016) that assumed time/scenario independent
603 internal variability, and Schlunegger et al., (2020) that used only high emission scenario internal variability from
604 four large ensembles to show there is strong agreement between LEs TOE both locally and spatially. Our results
605 argue for focusing observational efforts on the highly active regions in order to detect human influence on the ocean
606 carbon sink. Meanwhile, they imply that observational timeseries in quiescent regions, such as Ocean Station Papa
607 in the NE Pacific, need to interpret any observed trends with care, since internal variability tends to dominate over
608 human induced trends.
609

610

611



612

613 **Figure 6-** Time of emergence of the multi-model mean anomaly under different scenarios. White regions indicate
614 where the anthropogenic signal cannot be detected even towards the end of the century.

615

616 ~~Previous studies have largely presented a single time of emergence; however, the time of emergence strongly~~
617 ~~depends on the future scenario. The time of emergence~~Time of emergence strongly depends on the future scenario.
618 Schlunegger et al. (2020) show for two scenarios that modest (~10 yr) TOE differences between different ESMs
619 under strong anthropogenic forcing can evolve into pronounced (60+ yr) TOE differences with moderate
620 mitigation. Here, we make use of three scenarios including a strong-mitigation scenario and account for scenario
621 dependence of internal variability in our approximation using CanESM5. On average, scenarios with smaller forced
622 trends emerge later as the size of the forced trend is critical to the time of emergence (Fig. 2-a). The TOE is
623 earliest on average over the global ocean in ssp585, while it is later in ssp245, and later still in ssp126. The earlier
624 times of emergence are largely due to the stronger signal in ssp585, and weaker in ssp245 and ssp126 (Fig. 2-a),
625 consistent with the imposed changes in atmospheric CO₂ concentration. The exceptions are quiescent regions that
626 show earlier detectability for ssp126 compared to other scenarios; these exceptions are associated with larger (but
627 negative) anomalies in the latter half of the century under ssp126 which has negative emissions (compare panels
628 d-f, and g-i on Fig. 1). Internal variability does evolve somewhat differently for each scenario, but this is secondary
629 (Fig. B2-S2). Schlunegger et al. (2020) argues that variables such as air-sea CO₂ flux which are sufficiently
630 sensitive to emissions emerge early, prior to significant divergence among future scenarios. Consistent with this
631 result, our results indicate that there is broad agreement between scenarios in the TOE patterns, when considering
632 the highly active regions. Interestingly, our scenario-specific TOE shows that differences between scenario TOEs
633 is associated with how sensitive different regions are to emission scenarios. More specifically, comparison to the
634 maps of scenario uncertainty (Fig. 5) shows that TOE differs more across scenarios in regions where scenario

635 uncertainty is small, such as the aforementioned subtropics Ekman convergence regions. Elsewhere, the emergence
636 happens before scenarios diverge significantly. Our results suggest that under the rapidly rising atmospheric CO₂
637 concentrations seen in ssp585, the human signal in the ocean carbon sink will be detectable across much of the
638 global ocean over the coming few decades. However, under strong mitigation scenarios, such as ssp126, early
639 emergence (earlier than 2030) will only occur in isolated regions: while counter-intuitively, less percentage of the
640 global ocean remains non-emergent by 2100.

641 4. Conclusions

642 Ocean ~~carbon~~ uptake ~~as a result of the~~ increasing atmospheric CO₂ ~~concentration occurs mostly in the 21st century~~
643 is concentrated in a few ~~hotspot~~active regions with 70 percent of the total sink occurring in less than 40 percent of
644 the global ocean. We analyze the results from the CMIP6 multi-model mean for the current state of the ocean
645 (1995-2015), and the middle (2040-2060) and late (2080-2100) 21st century relative to the current state for three
646 scenarios. We show that future changes in the sink are projected to mostly take place within the same historical
647 ~~hotspot~~highly active regions. This result implies that known regions of high historical uptake, including the North
648 Atlantic and Southern Ocean, are the same regions to prioritize for observing the future evolution of the sink. Our
649 results extend the argument of Wang et al. (2016) that the historical state is a good predictor of the future state to
650 spatial patterns of change.

651
652 We show that the CMIP6 multi-model mean provides a consistent estimate of the spatial patterns of the sink, and
653 the trend in the sink (globally), compared to the observation-based data product dataset of Landschützer et al.
654 (2016). These results suggest the CMIP6 models are valid tools for understanding the past and future evolution of
655 the ocean carbon sink, particularly at broad spatial scales. A notable area of disagreement is that the Landschützer
656 et al. (2016) data shows larger decadal variability at the global scale than seen in any CMIP6 model. ~~We argue and~~
657 ~~the overestimation range of internal variability by this dataset is a plausible explanation, since at the regional scale,~~
658 ~~there is no such disagreement. This is in agreement with from CanESM5 large ensemble.~~ Gloege et al. (2021) ~~who~~
659 ~~showed~~shows that the SOM-FFN method overestimates the magnitude of decadal variability ~~by 21%~~ on the global
660 scale due to the amount of gap filling.

661
662 We have shown that the magnitude of uncertainty and its partitioning among different sources differs with scale
663 and location. On the global scale, scenario uncertainty is the largest source of uncertainty followed by model

664 uncertainty and internal variability. ~~However, as for CMIP6 models. These results are in agreement with previous~~
665 ~~studies form CMIP5 models (Lovenduski et al., 2016; Schlunegger et al., 2020).~~ As the scales of integration
666 (averaging) get finer, model and internal variability become the dominant sources, respectively. Testing the results
667 on two ocean ~~basins~~regions of about the same size, one in the NE Pacific and one in the NW Atlantic shows that -
668 while consistent with the results of the scale dependence analysis - the relative importance of the sources of
669 uncertainty also differs with location. ~~Notably, in hotspot~~Our test here extends the analysis Schlunegger et al.
670 ~~(2020) with a focus on the association of the location dependence with whether the regions have highly active~~
671 ~~carbon sinks. Notably, in highly active~~ regions, such as the NW Atlantic, scenario uncertainty is large, whereas in
672 more quiescent regions, such as the NE Pacific, internal variability is more significant. The dependence of internal
673 variability on the scenario with time is another interesting finding that could be the subject of future studies for a
674 better understanding of the driving mechanism and the degree of dependence on the future emissions and/or
675 concentrations.

676
677 The patterns of high future CO₂ uptake uncertainty are highly correlated with the patterns of historical uptake. The
678 correlation coefficients are highest for scenario uncertainty, indicating that the ~~hotspot~~highly active regions have
679 the potential for the sink to evolve according to the atmospheric CO₂ concentration, while the rest of the ocean
680 basins do not respond strongly to changes in atmospheric CO₂ represented by the different scenarios. This finding
681 has implications for assessment of the mitigations and effects of socioeconomic decisions. Our results here are
682 significant in that they show that regions of future uncertainty are largely associated with known regions of
683 significant historical uptake.

684
685 Patterns seen in the time-of-emergence have implications for planning observational campaigns for detection of a
686 signal. ~~(Schlunegger et al. 2019 & 2020).~~ Furthermore, there is reverse association between how sensitive a region
687 is to scenario differences (apparent in the scenario uncertainty patterns) and how sensitive the TOE is to scenarios.
688 Our results show that ~~there~~caution should be ~~caution~~ taken in interpreting the observed changes in regions such as
689 NE Pacific ~~(where active sampling is being done)~~ associated ~~with the late~~with late time of emergence of the signal
690 from the decadal (internal) variations. On the other hand, regions such as the Equatorial Pacific, the Gulf Stream
691 and Kuroshio and their extensions, and the Southern Ocean, should be the focus of consistent and expanded
692 sampling for detection of the forced signal. Additionally, the patterns in sources of uncertainty show that model
693 uncertainty is largest in the Southern Ocean, consistent with ~~previous studies.~~Frölicher et al., 2015. The sink in the
694 Southern Ocean is driven by complex mechanisms involving coupled ocean-atmosphere-ice interactions that

695 require better representation in ocean biogeochemical models. ~~If we wish to constrain and reduce future~~ Significant
696 progress in reducing uncertainties ~~in the ocean carbon sink, our~~ can be expected from new methods of bringing
697 together models and observations (Frolicher et al. 2016). Our results provide a motivation to focus modelling as
698 well as observational efforts on the known ~~hotspot~~ highly active regions of historical uptake.

699

700 Finally, we have shown that internal variability shows clear changes in time and depends on the scenario. The
701 emergence of Large Ensembles (LEs) allows for quantification of these variations if enough ensemble members
702 are available to fully capture internal variability using realizations that start from different initial conditions. Our
703 use of the CanESM5 LE allows for us to account for the nonstationary of internal variability in time, like in
704 Schlunegger et al. (2020) but with the advantage of also accounting for scenario dependence. Model
705 intercomparison indicates that ESMs show differences in natural variability (Schlunegger et al. 2020). Nonetheless,
706 our analysis of the global scale, of scale dependence, and of the patterns seen in Time of Emergence are consistent
707 with previous studies, despite the potential sensitivity to the use of CanESM5 LE. Our methodology to correct for
708 internal variability from model spread, without filtering or having a large ensemble for each ESM (which would
709 limit the number of ESMs that can be included and, consequently, underestimate model uncertainty) lays the
710 foundation for future studies when LEs are available from more ESMs and advocates for more modelling groups
711 to provide such LEs in order to achieve an even more robust estimate of internal variability as the mean across
712 different ESMs.

713

714 **Data Availability**

715 The data used in this study is part of the World Climate Research Programme's (WCRP) 6th Coupled Model
716 Intercomparison Project (CMIP6) open access data. For details on accessibility see section S1 in the Supplements.
717 The SOM-FFN data (Landschützer et al., 2017) from Landschützer (2016) can be accessed through the [National](https://www.nodc.noaa.gov/archive/arc0105/0160558/3.3/data/0-data/)
718 [Oceanographic Data Center](https://www.nodc.noaa.gov/archive/arc0105/0160558/3.3/data/0-data/) (NODC, <https://www.nodc.noaa.gov/archive/arc0105/0160558/3.3/data/0-data/>)
719 operated by the National Oceanic and Atmospheric Administration (NOAA) of the U.S. Department of Commerce.

720 **Author Contribution**

721 Parsa Gooya conducted the formal analysis, visualization, and original draft preparation. Conceptualization, and
722 methodology development and validation were a collaboration of the three authors, mainly developed by Parsa
723 Gooya with contributions from Neil Swart in development, validation, and revision and Roberta Hamme in
724 validation and revision. Neil Swart and Roberta Hamme provided supervision and reviewing and editing of the
725 manuscript and methodology. Funding acquisition was carried out by Roberta Hamme.

726 **Competing of interest**

727 The authors declare that they have no conflict of interest.

728 **Acknowledgments**

729 This work was supported by the Marine Carbon Sink project, funded by the Natural Sciences and Engineering
730 Research Council of Canada through the Advancing Climate Change Science in Canada program. We thank Jim
731 Christian for helpful suggestions on a draft of the manuscript.

733 **References**

- 734 Bopp, L., Lévy, M., Resplandy, L., and Sallée, J. B.: Pathways of anthropogenic carbon subduction in the global
735 ocean, *Geophys. Res. Lett.*, 42, 6416– 6423, doi:10.1002/2015GL065073, 2015.
- 736
- 737 Bushinsky, S. M., Landschützer, P., Rödenbeck, C., Gray, A. R., Baker, D., Mazloff, M. R., Resplandy, L., Johnson, K.
738 S., and Sarmiento, J. L.: Reassessing Southern Ocean air-sea CO₂ flux estimates with the addition of biogeochemical
739 float observations. *Global Biogeochemical Cycles*, 33, 1370– 1388. <https://doi.org/10.1029/2019GB006176>, 2019.
- 740
- 741 Canadell, J. G., Monteiro, P. M. S., Costa, M. H., Cotrim da Cunha, L., Cox, P. M., Eliseev, A. V., Henson, S., Ishii,
742 M., Jaccard, S., Koven, C., Lohila, A., Patra, P. K., Piao, S., Rogelj, J., Syampungani, S., Zaehle, S., and Zickfeld,
743 K.: Global Carbon and other Biogeochemical Cycles and Feedbacks. In *Climate Change 2021: The Physical Science
744 Basis. Contribution of Working Group I to the Sixth Assessment Report of the Intergovernmental Panel on Climate
745 Change* [Masson-Delmotte, V., Zhai, P., Pirani, A., Connors, S. L., Péan, C., Berger, S., Caud, N., Chen, Y., Goldfarb,
746 L., Gomis, M. I., Huang, M., Leitzell, K., Lonnoy, E., Matthews, J. B. R., Maycock, T. K., Waterfield, T., Yelekçi,
747 O., Yu, R., and B. Zhou (eds.)]. Cambridge University Press, Cambridge, United Kingdom and New York, NY, USA,
748 pp. 673–816, doi:10.1017/9781009157896.007, (2021).
- 749

750 Ciais, P. and Sabine, C.: Carbon and other biogeochemical cycles, in *Climate Change 2013: The Physical Science Basis*.
751 Contribution of Working Group I to the Fifth Assessment Report of the Intergovernmental Panel on Climate Change.
752 Cambridge Univ. Press, 2013.

753 Crisp, D., Dolman, H., Tanhua, T., McKinley, G. A., Hauck, J., Bastos, A., Sitch, S., Eggleston, S., and Aich, V.: How
754 well do we understand the land-ocean-atmosphere carbon cycle?, *Reviews of Geophysics*, 60,
755 e2021RG000736. <https://doi.org/10.1029/2021RG000736>, 2022.

756 Eyring, V., Bony, S., Meehl, G. A., Senior, C. A., Stevens, B., Stouffer, R. J., and Taylor, K. E.: Overview of the
757 Coupled Model Intercomparison Project Phase 6 (CMIP6) experimental design and organization, *Geosci. Model Dev.*,
758 9, 1937–1958, <https://doi.org/10.5194/gmd-9-1937-2016>, 2016.

759

760 Fay, A. R. and McKinley, G. A.: Global trends in surface ocean pCO₂ from in situ data. *Global Biogeochemical Cycles*,
761 27(2), 541–557, <https://doi.org/10.1002/gbc.20051>, 2013.

762

763

764 Friedrich, T., Timmermann, A., Abe-Ouchi, A., Bates, N. R., Chikamoto, M. O., and Church, M. J.: Detecting regional
765 anthropogenic trends in ocean acidification against natural variability. *Nat. Clim. Change*, 2, 167–171. doi:
766 10.1038/nclimate1372, 2012.

767

768 Friedlingstein, P., Jones, M. W., O'Sullivan, M., Andrew, R. M., Bakker, D. C. E., Hauck, J., Le Quéré, C., Peters, G.
769 P., Peters, W., Pongratz, J., Sitch, S., Canadell, J. G., Ciais, P., Jackson, R. B., Alin, S. R., Anthoni, P., Bates, N. R.,
770 Becker, M., Bellouin, N., Bopp, L., Chau, T. T. T., Chevallier, F., Chini, L. P., Cronin, M., Currie, K. I., Decharme, B.,
771 Djeuthouang, L., Dou, X., Evans, W., Feely, R. A., Feng, L., Gasser, T., Gilfillan, D., Gkritzalis, T., Grassi, G., Gregor,
772 L., Gruber, N., Gürses, Ö., Harris, I., Houghton, R. A., Hurtt, G. C., Iida, Y., Ilyina, T., Lujikx, I. T., Jain, A. K., Jones,
773 S. D., Kato, E., Kennedy, D., Klein Goldewijk, K., Knauer, J., Korsbakken, J. I., Körtzinger, A., Landschützer, P.,
774 Lauvset, S. K., Lefèvre, N., Lienert, S., Liu, J., Marland, G., McGuire, P. C., Melton, J. R., Munro, D. R., Nabel, J. E.
775 M. S., Nakaoka, S.-I., Niwa, Y., Ono, T., Pierrot, D., Poulter, B., Rehder, G., Resplandy, L., Robertson, E., Rödenbeck,
776 C., Rosan, T. M., Schwinger, J., Schwingshackl, C., Séférian, R., Sutton, A. J., Sweeney, C., Tanhua, T., Tans, P. P.,
777 Tian, H., Tilbrook, B., Tubiello, F., van der Werf, G., Vuichard, N., Wada, C., Wanninkhof, R., Watson, A., Willis, D.,
778 Wiltshire, A. J., Yuan, W., Yue, C., Yue, X., Zaehle, S., and Zeng, J.: Global Carbon Budget 2021, *Earth Syst. Sci. Data*
779 *Discuss.* [preprint], <https://doi.org/10.5194/essd-2021-386>, in review, 2021.

780

781

782 Frölicher, T. L., Sarmiento, J. L., Paynter, D. J., Dunne, J. P., Krasting, J. P., and Winton, M.: Dominance of the
783 Southern Ocean in anthropogenic carbon and heat uptake in CMIP5 models, *J. Clim.*, 28(2), 862– 886, 2015.

784

785 Frölicher, T. L., Rodgers, K. B., Stock, C. A., and Cheung, W. W. L.: Sources of uncertainties in 21st century projections
786 of potential ocean ecosystem stressors, *Global Biogeochem. Cycles*, 30, 1224– 1243, doi:10.1002/2015GB005338,
787 2016.

788

789 Graven, H. D., Gruber, N., Key, R., Khatiwala, S., and Giraud, X.: Changing controls on oceanic radiocarbon: New
790 insights on shallow-to-deep ocean exchange and anthropogenic CO₂ uptake, *J. Geophys. Res.-Oceans*, 117,
791 C10005, <https://doi.org/10.1029/2012JC008074>, 2012.

792

793 Gloege, L., McKinley, G. A., Landschützer, P., Fay, A. R., Frölicher, T. L., Fyfe, J. C., et al.: Quantifying errors in
794 observationally based estimates of ocean carbon sink variability. *Global Biogeochemical Cycles*, 35,
795 doi:10.1029/2020GB006788, 2021.
796

797 Gray, A. R., Johnson, K. S., Bushinsky, S. M., Riser, S. C., Russell, J.L., Wanninkhof, R., Williams, N. L., and
798 Sarmiento, J. L.: Autonomous biogeochemical floats detect significant carbon dioxide outgassing in the high-latitude
799 Southern Ocean, *Geophys. Res. Lett.*, 45, 9049–57, 2018.
800

801 Gruber, N., Landschützer, P., and Lovenduski, N. S.: The Variable Southern Ocean Carbon Sink, *Annual Review of*
802 *Marine Science*, 11:1, 159-186, 2019.
803

804 Hauck, J., Völker, C., Wolf-Gladrow, D. A., Laufkötter, C., Vogt, M., Aumont, O., Bopp, L., Buitenhuis, E. T., Doney,
805 S. C., Dunne, J., Gruber, N., Hashioka, T., John, J., Le Quéré, C., Lima, I. D., Nakano, H., Séférian, R., Totterdell, I.: On
806 the Southern Ocean CO₂ uptake and the role of the biological carbon pump in the 21st century, *Global Biogeochem.*
807 *Cycles*, 29, 1451– 1470, doi:10.1002/2015GB005140, 2015.
808

809 Hauck J., Zeising M., Le Quéré C., Gruber N., Bakker D. C. E., Bopp L., Chau T. T. T., Gürses Ö., Ilyina T.,
810 Landschützer P., Lenton A., Resplandy L., Rödenbeck C., Schwinger J. and Séférian R.: Consistency and Challenges in
811 the Ocean Carbon Sink Estimate for the Global Carbon Budget. *Front. Mar. Sci.* 7:571720. doi:
812 10.3389/fmars.2020.571720, 2020.
813

814 Hawkins, E. and Sutton, R.: The potential to narrow uncertainty in regional climate predictions. *Bull. Am. Meteorol.*
815 *Soc.*, 90:1095, 2009.
816

817 Hawkins, E. and Sutton, R. Time of emergence of climate signals. *Geophys. Res. Lett.* 39, L01702, 2012.
818
819

820 Joos, F. and Spahni, R.: Rates of change in natural and anthropogenic radiative forcing over the past 20,000 years.
821 *Proceedings of the National Academy of Sciences of the United States of America*, 105, 1425-30, 2008.
822
823

824 Kumar, D. and Ganguly, A. R.: Intercomparison of model response and internal variability across climate model
825 ensembles, *Clim. Dynam.*, 51, 207–219, <https://doi.org/10.1007/s00382-017-3914-4>, 2018.
826

827 Landschützer, P., Gruber, N., Haumann, F. A., Rödenbeck, C., Bakker, D. C., Van Heuven, S., Hoppema M., Metzl N.,
828 Sweeney C., Takahashi T., Tilbrook B., Wanninkhof R.: The reinvigoration of the Southern Ocean carbon sink. *Science*,
829 349(6253), 1221–1224, 2015.
830
831

832 Landschützer, P., Gruber, N., and Bakker, D. C. E.: Decadal variations and trends of the global ocean carbon sink, *Global*
833 *Biogeochem. Cycles*, 30, 1396– 1417, doi:10.1002/2015GB005359, 2016.
834
835

836 Landschützer, P., Gruber N., and Bakker, D.C.E.: An updated observation-based global monthly gridded sea surface
837 pCO₂ and air-sea CO₂ flux product from 1982 through 2015 and its monthly climatology (NCEI Accession 0160558),
838 Version 2.2, NOAA National Centers for Environmental Information, Dataset, 2017.
839
840

841 Laufkötter, C., Vogt, M., Gruber, N., Aita-Noguchi, M., Aumont, O., Bopp, L., Buitenhuis, E., Doney, S. C., Dunne, J.,
842 Hashioka, T., Hauck, J., Hirata, T., John, J., Le Quéré, C., Lima, I. D., Nakano, H., Seferian, R., Totterdell, I., Vichi, M.,
843 and Völker, C.: Drivers and uncertainties of future global marine primary production in marine ecosystem models,
844 *Biogeosciences*, 12, 6955–6984, <https://doi.org/10.5194/bg-12-6955-2015>, 2015.

845
846 Lehner, F., Deser, C., Maher, N., Marotzke, J., Fischer, E. M., Brunner, L., Knutti, R., and Hawkins, E.: Partitioning
847 climate projection uncertainty with multiple large ensembles and CMIP5/6, *Earth Syst. Dynam.*, 11, 491–508,
848 <https://doi.org/10.5194/esd-11-491-2020>, 2020.

849
850 Lorenz E. N.: The predictability of a flow which possesses many scales of motion., *Tellus*, ;21:19, 1969.

851
852 Lovenduski, N. S., Gruber, N., Doney, S. C., and Lima, I. D.: Enhanced CO2 outgassing in the Southern Ocean from a
853 positive phase of the Southern Annular Mode. *Global Biogeochemical Cycles*, 21(2).
854 <https://doi.org/10.1029/2006GB002900>, 2007.

855
856
857 Lovenduski, N. S., McKinley, G. A., Fay, A. R., Lindsay, K., and Long, M. C.: Partitioning uncertainty in ocean carbon
858 uptake projections: Internal variability, emission scenario, and model structure, *Global Biogeochem.*
859 *Cycles*, 30, 1276– 1287, 2016.

860
861
862 Masson-Delmotte, V., P. Zhai, A. Pirani, S.L. Connors, C. Péan, S. Berger, N. Caud, Y. Chen, L. Goldfarb, M.I. Gomis,
863 M. Huang, K. Leitzell, E. Lonnoy, J.B.R. Matthews, T.K. Maycock, T. Waterfield, O. Yelekçi, R. Yu, and B. Zhou
864 (eds.): IPCC, 2021: Summary for Policymakers. In: *Climate Change 2021, The Physical Science Basis. Contribution of*
865 *Working Group I to the Sixth Assessment Report of the Intergovernmental Panel on Climate Change. In Press.*

866
867
868 McKinley G. A., Pilcher D. J., Fay A. R., Lindsay K., Long M. C., and Lovenduski N. S.: Timescales for detection of
869 trends in the ocean carbon sink. *Nature*, 530(7591), 469-72. doi: 10.1038/nature16958. PMID: 26911782, 2016.

870
871 McKinley, G. A., Fay, A. R., Lovenduski, N. S., and Pilcher, D.: Natural variability and anthropogenic trends in the
872 ocean carbon sink. *Annual Review of Marine Science*, 9(1), 125–150. [https://doi.org/10.1146/annurev-marine-010816-](https://doi.org/10.1146/annurev-marine-010816-060529)
873 [060529](https://doi.org/10.1146/annurev-marine-010816-060529), 2017.

874
875 McKinley, G. A., Fay, A. R., Eddebbar, Y. A., Gloege, L., and Lovenduski, N. S.: External forcing explains recent
876 decadal variability of the ocean carbon sink. *AGU Advances*, 1,
877 e2019AV000149. <https://doi.org/10.1029/2019AV000149>, 2020.

878
879
880 Riahi, K., van Vuuren, D. P., Kriegler, E., Edmonds, J., O’Neill, B. C., Fujimori, S., Bauer, N., Calvin, K., Dellink, R.,
881 Fricko, O., Lutz, W., Popp, A., Cuaresma, J. C., KC, S., Leimbach, M., Jiang, L., Kram, T., Rao, S., Emmerling, J., Ebi,
882 K., Hasegawa, T., Havlik, P., Humpenöder, F., Aleluia Da Silva, L., Smith, S., Stehfest, E., Bosetti, V., Eom, J., Gernaat,
883 D., Masui, T., Rogelj, J., Strefler, J., Drouet, L., Krey, V., Luderer, G., Harmsen, M., Takahashi, K., Baumstark, L.,
884 Doelman, J. C., Kainuma, M., Klimont, Z., Marangoni, G., Lotze-Campen, H., Obersteiner, M., Tabeau, A., and Tavoni,
885 M.: The Shared Socioeconomic Pathways and their energy, land use, and greenhouse gas emissions implications: An
886 overview, *Global Environmental Change*, Volume 42, 153-168, ISSN 0959-3780,
887 <https://doi.org/10.1016/j.gloenvcha.2016.05.009>, 2017.

888

889 Ridge, S. M. and McKinley, G. A.: Ocean carbon uptake under aggressive emission mitigation, *Biogeosciences*, 18,
890 2711–2725, <https://doi.org/10.5194/bg-18-2711-2021>, 2021.

891

892 Rodgers, K. B., Lin, J. and Frolicher, T. L.: Emergence of multiple ocean ecosystem drivers in a large ensemble suite
893 with an Earth system model. *Biogeosciences*, 12, 3301–3320, 2015.

894

895 Roy, T., L. Bopp, M. Gehlen, B. Schneider, P. Cadule, T. L. Frölicher, J. Segschneider, J. Tjiputra, C. Heinze, and F.
896 Joos: Regional impacts of climate change and atmospheric CO₂ on future ocean carbon uptake: A multimodel linear
897 feedback analysis, *J. Clim.*, 24(9), 2300–2318, 2011.

898

899 Santer, B.D., P.W. Thorne, L. Haimberger, K.E. Taylor, T.M.L. Wigley, J.R. Lanzante, S. Solomon, M. Free, P.J.
900 Gleckler, P.D. Jones, T.R. Karl, S.A. Klein, C. Mears, D. Nychka, G.A. Schmidt, S.C. Sherwood, and F.J. Wentz:
901 Consistency of modelled and observed temperature trends in the tropical troposphere. *Int. J. Climatol.*, 28, 1703-1722,
902 doi:10.1002/joc.1756, 2008.

903

904 Sarmiento, J. L., Hughes, T. M. C., Stouffer, R. J., and Manabe, S.: Simulated response of the ocean carbon cycle to
905 anthropogenic climate warming. *Nature*, 393(6682), 245–249. <https://doi.org/10.1038/30455>, 1998.

906

907 Schlunegger, S., Rodgers, K. B., Sarmiento, J. L., Frölicher, T. L., Dunne, J. P., Ishii, M., and Slater, R.: Emergence of
908 anthropogenic signals in the ocean carbon cycle. *Nature Climate Change*, 9(9), 719–725.
<https://doi.org/10.1038/s41558-019-0553-2>, 2019.

909

910 Schlunegger, S., Rodgers, K. B., Sarmiento, J. L., Ilyina, T., Dunne, J. P., Takano, Y., Christian, J. R., Long, M. C.,
911 Frölicher, T. L., Slater, R., and Lehner, F.: Time of Emergence and Large Ensemble Intercomparison for Ocean
912 Biogeochemical Trends. *Global Biogeochemical Cycles*, 34(8), e2019GB006453.
<https://doi.org/https://doi.org/10.1029/2019GB006453>, 2020.

913

914 Somerville, R.C.J.: The predictability of weather and climate. *Climatic Change* 11, 239–246,
<https://doi.org/10.1007/BF00138802>, 1987.

915

916 Sutton AJ, Wanninkhof R, Sabine CL, Feely RA, Cronin MF, Weller RA. 2017. Variability and trends in surface
917 seawater pCO₂ and CO₂ flux in the Pacific Ocean. *Geophys Res Lett*, 44(11): 5627–5636. doi:
10.1002/2017GL073814

918

919 Takahashi T., Sutherland S. C., Feely R.A., Wanninkhof R.: Decadal change of the surface water pCO₂ in the North
920 Pacific: A synthesis of 35 years of observations. *J Geophys Res*, 111(C7): C07S05. doi: 10.1029/2005JC003074, 2006.

921

922 Tebaldi C. and Knutti R.: The use of the multimodel ensemble in probabilistic climate projections. *Phil. Trans. R. Soc.*
923 *A.*, 365, 2053–2075, 2007.

924

925 Terhaar, J., Frölicher, T. L., and Joos, F.: Southern Ocean anthropogenic carbon sink constrained by sea surface
926 salinity. *Science Advances*, 7(18), eabd5964. <https://doi.org/10.1126/sciadv.abd5964>, 2021.

927

928 Tjiputra, J. F., Olsen, A., Bopp, L., Lenton, A., Pfeil, B., Roy, T., Segschneider, J., Totterdell, I., and Heinze, C.: Long-
929 term surface pCO₂ trends from observations and models, *Tellus B.*, 66, 23083, 2014.
930
931 Toyama, K., Rodgers, K. B., Blanke, B., Iudicone, D., Ishii, M., Aumont, O., and Sarmiento, J. L.: Large Reemergence
932 of Anthropogenic Carbon into the Ocean's Surface Mixed Layer Sustained by the Ocean's Overturning Circulation, *J.*
933 *Climate*, 30, 8615–8631, <https://doi.org/10.1175/JCLI-D-16-0725.1>, 2017.
934
935
936 Wang, L., Huang, J., Luo, Y., and Zhao, Z.: Narrowing the spread in CMIP5 model projections of air-sea CO₂
937 fluxes. *Scientific Reports*, 6(1), 37548. <https://doi.org/10.1038/srep37548>, 2016.

938
939 Williams, N. L., Juranek, L. W., Feely, R. A., Russell, J. L., Johnson, K. S., and Hales, B.: Assessment of the carbonate
940 chemistry seasonal cycles in the Southern Ocean from persistent observational platforms. *J. Geophys. Res. Oceans*,
941 123,4833–52, 2018.
942